Prepared for submission to JCAP

Baryonic effects for weak lensing. Part I. Power spectrum and covariance matrix

Aurel Schneider,[a,b] **Nicola Stoira,**[b] **Alexandre Refregier,**[b] **Andreas J. Weiss,**[c] **Mischa Knabenhans,**[a] **Joachim Stadel,**[a] **and Romain Teyssier**[a]

[a]Institute for Computational Science, University of Zurich, Winterthurerstrasse 190, 8057 Zurich, Switzerland.

[b]Institute for Particle Physics and Astrophysics, ETH Zurich, Wolfgang Pauli Strasse 27, 8093 Zurich, Switzerland.

[c]Space Research Institute, Austrian Academy of Sciences, Schmiedlstrasse 6, 8042 Graz, Austria

E-mail: aurel.schneider@uzh.ch

Abstract. Baryonic feedback effects lead to a suppression of the weak lensing angular power spectrum on small scales. The poorly constrained shape and amplitude of this suppression is an important source of uncertainties for upcoming cosmological weak lensing surveys such as Euclid or LSST. In this first paper in a series of two, we use simulations to build a Euclid-like tomographic mock data-set for the cosmic shear power spectrum and the corresponding covariance matrix, which are both corrected for baryonic effects following the *baryonification* method of Schneider et al. [1]. In addition, we develop an emulator to obtain fast predictions of the baryonic power suppression, allowing us to perform a likelihood inference analysis for a standard ΛCDM cosmology with both cosmological and astrophysical parameters. Our main findings are the following: (i) ignoring baryonic effects leads to a greater than 5σ bias on the cosmological parameters Ω_m and σ_8; (ii) restricting the analysis to the largest scales, that are mostly unaffected by baryons, makes the bias disappear, but results in a blow-up of the Ω_m-σ_8 contour area by more than a factor of 10; (iii) ignoring baryonic effects on the covariance matrix does not significantly affect cosmological parameter estimates; (iv) while the baryonic suppression is mildly cosmology dependent, this effect does not noticeably modify the posterior contours. Overall, we conclude that including baryonic uncertainties in terms of nuisance parameters results in unbiased and surprisingly tight constraints on cosmology.

Contents

1 Introduction

Within the next few years, large-scale weak lensing surveys will provide unprecedented data to study the cosmological model (ΛCDM) and its unknown cold dark matter and dark energy components. The range of scales probed by future surveys like Euclid[1], LSST[2], and WFIRST[3] will include the highly nonlinear regime of structure formation that has to be modelled with numerical simulations.

Over the last decades, gravity-only N-body simulations have been continuously developed towards higher particle numbers and improved accuracy. As a result, they are now close to approaching percent-level precision regarding the non-linear clustering signal [e.g. Refs. 2–4]. However, N-body simulations are time-consuming and cosmological parameter estimation requires fast predictors that can be used to scan the high-dimensional parameter space

[1] `https://www.euclid-ec.org/`
[2] `https://www.lsst.org/`
[3] `https://wfirst.gsfc.nasa.gov/`

of ΛCDM. The current approach of cosmological inference therefore relies on simulations to adjust fitting functions and regression routines based for example on the halo model [5–8], on direct emulation techniques [9–11], or on neural networks [12–15].

However, it has become increasingly evident over the last few years that baryonic processes (which are ignored in gravity-only N-body simulations and associated regression techniques) have a significant effect on current and future weak-lensing observations. Several hydrodynamical simulations which include feedback effects from active galactic nuclei (AGN) and supernova explosions have shown that the clustering signal is affected by 10-30 percent at the nonlinear scales [16–23]. Similar effects have been found using the more analytical and physically intuitive approach of the halo model [24–27]. A short review about the baryonic effects and their connection to cosmology is provided in Chisari et al. [28].

An alternative model halfway between the halo model and simulations has recently been introduced in the Refs. [1, 29]. This *baryonification* approach relies on an empirical parametrisation of halo profiles (including gas, stars, and dark matter) and modifies the output of a gravity-only N-body simulation by slightly displacing particles around halo centres. The advantage of *baryonifying* N-body simulations is that the baryonic effects are empirically parametrised, making it possible to perform many fast realisations of the nonlinear cosmic density field with varying baryonic parameters. As a result it is possible to go beyond the power spectrum, studying for example weak-lensing maps via peak statistics [30] or a deep-learning approach [31].

The present paper is the first in a series of two, where we build upon the *baryonification* model of Ref. [1] to perform a cosmological forecast analysis for the cosmic shear power spectrum of a stage-IV weak-lensing survey. We construct mock observations based on a Euclid-like survey configuration with a covariance matrix obtained from a suite of *baryonified* N-body simulations. This allows us to perform a number of Monte-Carlo Markov Chain runs to study the effects of baryons on the posterior contours of cosmological and baryonic parameters.

There are several questions we want to address with this paper: (i) To what accuracy will it be possible to measure cosmological parameters of the ΛCDM model if we marginalise over baryonic uncertainties? (ii) By how much will the errors decrease if we fix the baryonic parameters to their true values, implying that they can be constrained with other observations? (iii) How much constraining power do we lose if we only rely on data from large scales that remain unaffected by baryons? (iv) What is the bias introduced if we analyse all the data but completely ignore the effects of baryons in the prediction pipeline? Next to these main questions, we also check the validity of several simplifying assumptions, such as ignoring baryons in the covariance matrix and keeping baryonic effects decoupled from cosmology. Finally, we also investigate the effects of additional freedom in the redshift dependence of the baryonic suppression signal.

All the results from the present paper assume a five-parameter ΛCDM cosmology where neutrinos are set to be massless. A more realistic setup, including massive neutrinos and several extensions beyond the ΛCDM framework, will be discussed in the second paper of this series [see Ref. 32].

The present paper is structured as follows: In Sec. 2 we revisit the *baryonification* approach and we present the *baryonic emulator* that allows us to speed up the calculations, making it fit for cosmological inference. In Sec. 3 we present our mock data-set including the covariance matrix which is based on a suite of simulations. Sec. 4 describes the results of our parameter inference for both the cosmological and the baryonic parameters. Finally, we dis-

cuss simplifying model assumptions in Sec. 5 and we conclude in Sec. 6. The Appendices A.1 and A.2 provide further details on the construction and the testing of the baryonic emulator.

2 Baryonic effects on the matter power spectrum

In this section, we review the *baryonic correction model* developed in Schneider et al. [1, henceforth S19] and we present the *baryonic emulator* built upon this model. The latter is required to speed up the prediction pipeline in order to perform Markov-Chain Monte-Carlo (MCMC) sampling for cosmological parameter estimates.

2.1 Summarising the baryonic correction model

The baryonic correction (BC) model consists of a numerical routine which aims to perturb gravity-only N-body simulations in order to account for the effects of baryonic feedback on the large-scale structure of the universe. The idea of the model is to displace simulation particles around each halo so that the original NFW profile ($\rho_{\rm nfw}$) is transformed into a final baryon-dark matter profile ($\rho_{\rm bcm}$), i.e.,

$$\rho_{\rm nfw}(r) \quad \longrightarrow \quad \rho_{\rm bcm}(r) = \rho_{\rm clm}(r) + \rho_{\rm gas}(r) + \rho_{\rm cga}(r), \tag{2.1}$$

where the latter consists of a central galactic (cga), a gas, and a collisionless matter (clm) component. Note that $\rho_{\rm clm}$ is dominated by dark matter but also contains satellite galaxies and intracluster stars. We now summarise the different components that go into the above relation. More details about the parametrisation and its comparison to observations can be found in S19 [1].

- The stellar profile of the central galaxy ($\rho_{\rm cga}$) is described by the truncated power law

$$\rho_{\rm cga}(r) \propto \frac{f_{\rm cga}(M)}{r^2} \exp\left[-\left(\frac{r}{2R_h}\right)^2\right], \qquad R_h = 0.015 \times r_{200}. \tag{2.2}$$

  The above relation only provides an approximate fit to realistic galaxies. Note, however, that the shape of the stellar profile has no influence on the clustering at scales relevant for weak lensing. The fractions of stars in the central galaxy ($f_{\rm cga}$) and the total stellar fraction ($f_{\rm star}$), including satellite galaxies and stars corresponding to the intra-cluster light ($f_{\rm sga}$) are defined as

$$f_{\rm cga} = 0.09 \left(\frac{M}{M_s}\right)^{-\eta_{\rm cga}}, \qquad f_{\rm star} = f_{\rm cga} + f_{\rm sga} = 0.09 \left(\frac{M}{M_s}\right)^{-\eta_{\rm star}}, \tag{2.3}$$

  where $M_s = 2.5 \times 10^{11}$ $\mathrm{M}_\odot/\mathrm{h}$ and where $\eta_{\rm star}$ and $\eta_{\rm cga}$ are free model parameters. For consistency reasons, we impose $\eta_{\rm cga} > \eta_{\rm star}$ and $M > 2.5 \times 10^{11}$ $\mathrm{M}_\odot/\mathrm{h}$. In principle, it would be straight forward to extend these relations to smaller halo masses by introducing a break in the stellar fractions below M_s [see e.g. Ref. 33]. Note, however, that the cosmological clustering signal of stage-IV weak lensing surveys is only affected by haloes above $M \sim 10^{12}$ $\mathrm{M}_\odot/\mathrm{h}$ [3].

- The collisionless matter profile ($\rho_{\rm clm}$), consisting of the dominant dark matter component plus satellite galaxies (including intra-cluster stars), is given by

$$\rho_{\rm clm}(r) = (\Omega_{\rm dm}/\Omega_m + f_{\rm sga})\, \rho_{\rm nfw}(r). \tag{2.4}$$

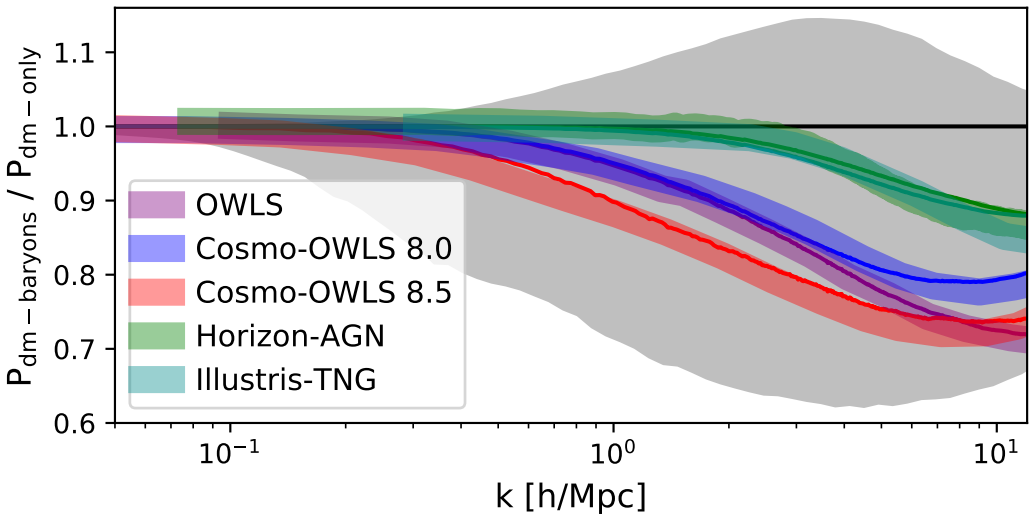

Figure 1. Comparison between the baryonic correction (BC) model (coloured lines) and various hydrodynamical simulations (coloured bands) from the literature [18–20, 24]. Note that the BC model parameters are not fitted to the power spectrum but to the gas and stellar fractions of each simulation. See S19 [1] for more details. The grey area in the background shows the prior range assumed in this paper.

This profile is furthermore allowed to react to the other components via the adiabatic relaxation prescription of Ref. [34]. A detailed description of this procedure is given in S19.

- Finally, the gas profile ($\rho_{\rm gas}$) is described by the relation

$$\rho_{\rm gas} \propto \frac{f_{\rm gas}}{(1+r/r_{\rm co})^{\beta}[1+(r/r_{\rm ej})^2]^{(7-\beta)/2}}, \qquad \beta = 3 - \left(\frac{M_c}{M}\right)^{\mu} \tag{2.5}$$

where $r_{\rm co} = 0.1 \times r_{200}$ and

$$r_{\rm ej} \equiv \theta_{\rm ej} \times r_{200}. \tag{2.6}$$

The gas fraction is obtained by subtracting the stellar fraction from the cosmic baryon fraction $f_b = \Omega_b/\Omega_m$, i.e.,

$$f_{\rm gas} = f_b - f_{\rm star}. \tag{2.7}$$

Note that the slope of the gas profile (described by the parameter β) is assumed to be mass-dependent with a shallower slope for galaxy-groups compared to clusters. Eq. (2.5) has been shown in S19 to be in good agreement with X-ray observations.

The parametrisation of the BC model summarised above has five free parameters, three related to the gas profile (M_c, μ, $\theta_{\rm ej}$) and two related to the stellar fractions ($\eta_{\rm cga}$, $\eta_{\rm star}$). The model is furthermore sensitive to the cosmic baryon fraction f_b, which we will show later on to affect the baryonic suppression signal of the matter power spectrum.

While the baryon correction method consists of an approximative approach based on outputs of gravity-only N-body simulations, it is in good agreement with full hydrodynamical

simulations. In S19 it is shown that if the BC model parameters are tuned to reproduce the gas and stellar fraction of a given hydrodynamical simulation, then the baryonic suppression effects on the matter power spectrum can be predicted with an accuracy of 2 percent or better up to $k = 10$ h/Mpc.

Fig. 1 shows a comparison of the power spectra from the baryonic correction model and the hydrodynamical simulations OWLS [24], Cosmo-OWLS [18], Horizon-AGN [20], and Illustris-TNG [19]. As explained above, the BC model parameters M_c, β, $\eta_{\rm cga}$, and $\eta_{\rm sga}$ are not fitted to reproduce the power suppression, but they are selected to match the gas and stellar fractions within r_{500} of the corresponding simulation. As the remaining parameter $\theta_{\rm ej}$ cannot be well constrained with gas fractions at only one enclosed mass scale, it is set to the fiducial value of $\theta_{\rm ej} = 4$. The predictions from the BC model are shown as coloured lines, while the results from the hydrodynamical simulations are plotted as broad coloured bands. The good agreement between model and simulations is highly non-trivial and illustrates how well the BC model is able to capture the baryonic effects on the large-scale structure of the universe[4].

The grey area shown in Fig. 1 will be discussed in more detail in Sec. 4. It represents the selected prior-range of the baryonic model parameters. This prior is conservative enough to include all known results from hydrodynamical simulations and describes the current uncertainties of baryonic effects on the cosmological clustering signal.

2.2 Cosmology-dependence of the baryonic effects

So far, all weak-lensing cosmological studies that included baryonic effects have implicitly assumed them to be independent of cosmology [see e.g. Refs. 35–39]. For the case of the cosmic shear power spectrum, this means for example that a cosmology-independent baryonic correction term can be simply multiplied to the dark-matter-only prediction of the matter power spectrum, considerably simplifying the analysis. In this section, we check the validity of this assumption by investigating potential correlations between the baryonic suppression effect and individual cosmological parameters.

We start by running one cosmological gravity-only N-body simulation assuming a standard 5-parameter ΛCDM cosmology (with massless neutrinos) with $\Omega_m = 0.315$, $\Omega_b = 0.049$, $h_0 = 0.674$, $n_s = 0.96$, $\sigma_8 = 0.811$ before calculating the matter power spectrum at $z = 0$. We then apply the baryonification method (with default parameter values of $M_c = 10^{14}$ $\mathrm{M}_\odot$/h, $\mu = 0.4$, $\theta_{\rm ej} = 4$, $\eta_{\rm cga} = 0.3$, and $\eta_{\rm cga} = 0.6$) and determine the ratio of the power spectrum with and without baryonic correction. As a next step, we run more N-body simulations where we vary each if the cosmological parameters individually while keeping the other parameters unchanged. For each of these simulations, we again determine the ratio of the power spectrum. We investigate the parameter ranges of $\Omega_m \in [0.24, 0.35]$, $\Omega_b \in [0.038, 0.055]$, $h \in [0.62, 0.77]$, $n_s \in [0.92, 1.00]$, and $\sigma_8 \in [0.78, 0.84]$.

In Fig. 2 we plot the resulting ratios of the power spectra with and without baryon correction for different values of the individual cosmological parameters. The top panels show that neither varying h_0, σ_8, nor n_s does significantly affect the spoon-like baryonic signal. The bottom-left and centre panels, on the other hand, show that varying Ω_b or Ω_m

[4]It is of course also possible to directly fit the BC model parameters to the relative power spectrum shown in Fig. 1. In this case we would obtain an even better agreement between the BC model and simulations. As a consequence, however, the baryonic parameter would lose their physical meaning. It would still be possible to use them as nuisance parameters in a weak-lensing cosmological inference analysis, but the direct connection to X-ray gas fraction (as shown in S19) would not be valid anymore.

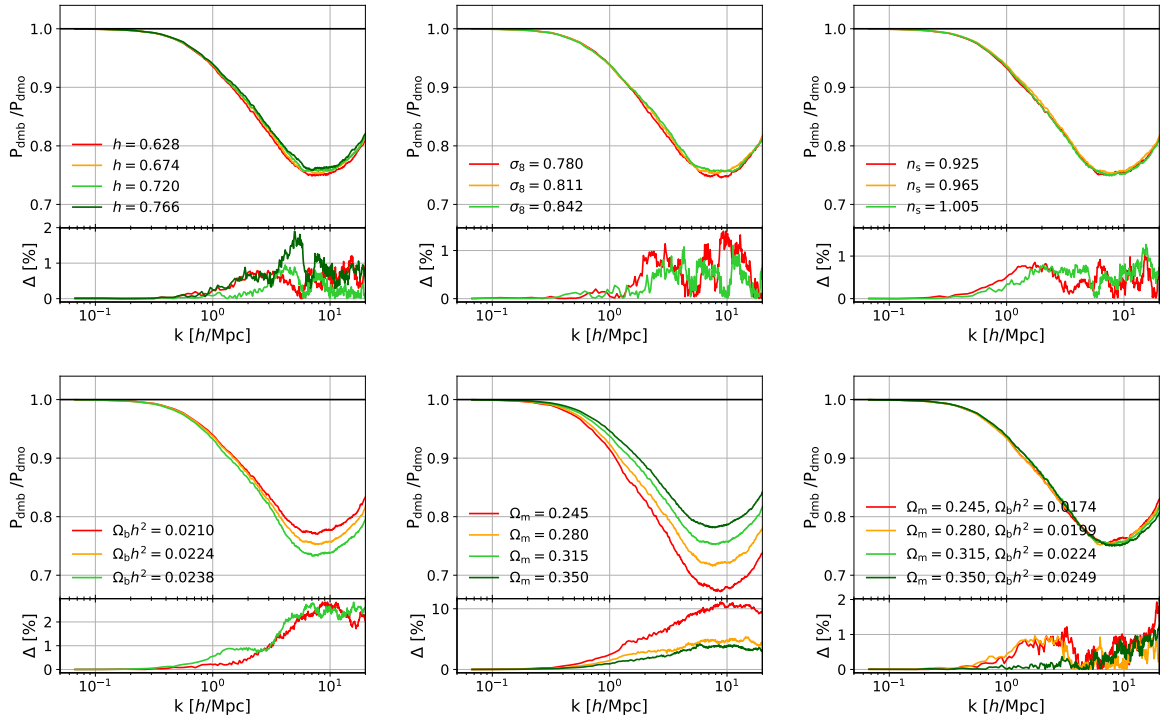

Figure 2. Cosmology-dependence of the baryonic suppression effect on the power spectrum, assuming a baryonic correction model with fixed parameters $M_c = 10^{14}$ $M_\odot/h$, $\mu = 0.4$, $\theta_{ej} = 4.0$, $\eta_{star} = 0.3$, and $\eta_{cga} = 0.6$. Values of individual cosmological parameters are labelled, all the other parameters are kept at their default values of $\Omega_m = 0.315$, $\Omega_b = 0.049$, $h_0 = 0.674$, $n_s = 0.96$, $\sigma_8 = 0.811$. Fractional differences to the default cosmology (Δ in percent) are shown in the corresponding sub-panels.

has a direct influence on the amplitude of the baryonic suppression. Finally, the bottom-right panel reveals that simultaneously changing Ω_b and Ω_m while keeping the baryon fraction $f_b = \Omega_b/\Omega_m$ fixed has no visible effect on the ratio of the power spectrum. We therefore conclude that the amplitude of the baryon effect is directly dependent on the comic baryon fraction f_b, but largely independent of other cosmological parameters.

The relation between baryonic feedback effects and the cosmic baryon fraction is not surprising. It is a simple consequence of the fact that feedback effects can have a larger influence on cosmological structure formation, if there is more gas compared to the total amount of matter. Regarding the baryonic correction model, the direct influence of the cosmic baryon fraction is visible in Eq. (2.5) and Eq. (2.7). A larger f_b automatically leads to a stronger influence of the gas profile and therefore potentially stronger baryonic effects.

The dependence between the baryonic feedback effects and the cosmic baryon fraction is a generic feature that is not restricted to the baryonic correction model. For example, it is also visible when comparing runs from the BAHAMAS simulations [40] that are based on the same AGN feedback implementation but different cosmologies. The change of the baryonic suppression effect on the BAHAMAS power spectra when going from `WMAP9` [41] to `Planck13` [42] can indeed be directly related to the corresponding shifts in Ω_m and Ω_b [see e.g. Fig. 6 in Ref. **?**]. Note that the same direct relation between cosmology and baryonic suppression effect can also be observed when comparing the power spectra from OWLS and cosmo-OWLS

Parameter Description	Acronym	Emulator Range
Gas parameter 1 (related to the slope of the gas profile)	$\log M_c$	12.7, 16.7
Gas parameter 2 (related to the slope of the gas profile)	μ	0.1, 1
Gas parameter 3 (related to the maximum gas ejection)	$\theta_{\rm ej}$	2, 8
Stellar parameter 1 (related to the total stellar fraction)	$\eta_{\rm star}$	0.2, 0.4
Stellar parameter 2 (related to the central galactic stellar fraction)	$\eta_{\rm cga}$	0.5, 0.7
Cosmic baryon fraction	f_b	0.13, 0.21
Redshift	z	0, 2

Table 1. Descriptions and ranges of the model parameters from the *baryonic emulator*. The cosmic baryon fraction is emulated between $f_b = 0.13-0.21$. Outside of this range and within $f_b = 0.05-0.5$, it is approximated using Eq. (2.9).

(which are based on `WMAP3` [43] and `WMAP7` [44] cosmologies, respectively).

All N-body simulations described in this section were run with the code `Pkdgrav3` [45, 46] assuming a box length of $L = 256$ Mpc/h and a particle number of $N = 512^3$. This box-length and resolution have been shown to be sufficient for converged ratios of the power spectrum at the percent level [see Ref. 29]. For the halo finding (which is a necessary step of the baryonification procedure) we used the `AHF` code described in Ref. [47].

2.3 Emulation of model parameters

In order to perform cosmological parameter inference, we require a fast pipeline to predict the tomographic cosmic shear power spectrum. This is only possible if we have a regression routine for the power suppression caused by baryonic effects that can be included into a MCMC sampling routine. The method should allow us to vary both the free baryonic parameters and the cosmological baryon fraction which affects the signal as established in the previous section.

Following the example of the `EuclidEmulator` [10], we construct an emulator for the baryonic suppression signal

$$S_{\rm BCM}(k,z) \equiv \frac{P_{\rm dmb}(k,z)}{P_{\rm dmo}(k,z)}, \tag{2.8}$$

where $P_{\rm dmo}(k,z)$ and $P_{\rm dmb}(k,z)$ are the absolute power spectra of the uncorrected (dark-matter-only) and the *baryonified* (dark-matter-baryon) density field. We thereby include the cosmological scales $k \leq 10$ h/Mpc and the redshift range $z \in [0,2]$. We start by building a training set (i.e. the experimental design) using a optimised latin hypercube sampling (LHS) strategy with 1000 points in the 6 dimensional parameter space and for five fixed redshift values $z = \{0, 0.5, 1, 1.5, 2\}$.

At each sample point of the experimental design, we then apply the baryonic correction model, generating a vector in k for $S_{\rm BCM}$. We do not run separate N-body simulations for this step, which considerably speeds up the process and allows us to go to a large experimental design. This is an approximation that is only accurate if changing the cosmology of the underlying N-body simulation has no (or very little) effect on the suppression signal. In Fig. 2 we have shown that this is indeed the case regarding the parameters h_0, σ_8, and n_s. For the remaining parameters Ω_m and Ω_b, the situation is more complicated. While Fig. 2 clearly shows that they do have an effect on $S_{\rm BCM}$, it is unclear wether this is entirely due to the parametrisation of the BC model or also due to the underlying simulation. In Appendix A.1, we further investigate the provenance of the cosmology dependence on $S_{\rm BCM}$, showing

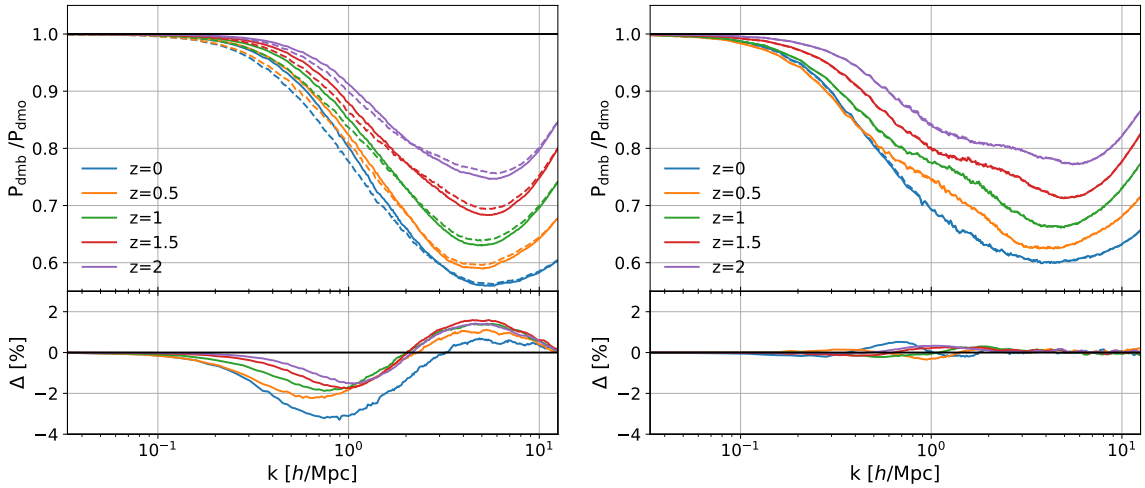

Figure 3. Baryonic power suppression from the *baryonic emulator* (dashed lines) and directly from the *baryonic correction model* (solid) for two test sample points in the 6-dimensional parameter space. The left-hand and right-hand panels show sample point 0 and 1, respectively. The parameter values of the two sample points together with the remaining points of the test sample are listed in Table 3 of Appendix A.2. More comparison results from the test sample are shown in Fig. 13.

that using simulations with different values of Ω_m while keeping the BC model parameters fixed, does not lead to substantial changes of $S_{\rm bcm}$. This confirms that using one single N-body simulation with fixed cosmology for the experimental design only introduces sub-percent errors for parameter values within the range of the emulator.

Once the experimental design is established, we construct the baryonic emulator using the uncertainty quantification software `UQLab` [48] which follows a spectral decomposition method called polynomial chaos expansion. The algorithm generates a surrogate model which can be evaluated for an arbitrary point in the parameter space. More details on the emulation technique can be found in Ref. [10].

The ranges for each of the six emulated parameters are given in Table 1. Note that we do not emulate the redshift parameter but we use direct interpolation at each k-mode instead. In the Appendix A.2 we show that this interpolation strategy results gives accurate results at all redshifts between $z = 0 - 2$. The f_b parameter is emulated between the values 0.13 and 0.21. Beyond this range we use the approximate relations

$$S_{\rm BCM}(k,z|f_b) = S_{\rm BCM}(k,z|f_b = 0.13)^{(f_b/0.13)^{1.2}}, \quad \text{for } \mathrm{f_b} < 0.13 \tag{2.9}$$
$$S_{\rm BCM}(k,z|f_b) = S_{\rm BCM}(k,z|f_b = 0.21)^{(f_b/0.21)^{1.2}}, \quad \text{for } \mathrm{f_b} > 0.21$$

We have checked that this provides a good fit to the simulation-based results. Note furthermore, that the posteriors of the resulting inference analysis shown in Sec. 4 (assuming either free or fixed baryonic parameters and including all scales of the mock sample) lie within the range of the emulator where the above approximation does not apply.

In order to test the baryonic emulator, we again use the optimised LHS method to assign six sample points in the parameter space, comparing the power suppression from the emulator with the one directly obtained from the *baryonification* method. In Fig. 3 we show a comparison from two of the six sampling points, the other four are plotted in Fig. 13 of Appendix A.2. The upper part of the figure represents the expected (continuous line) and

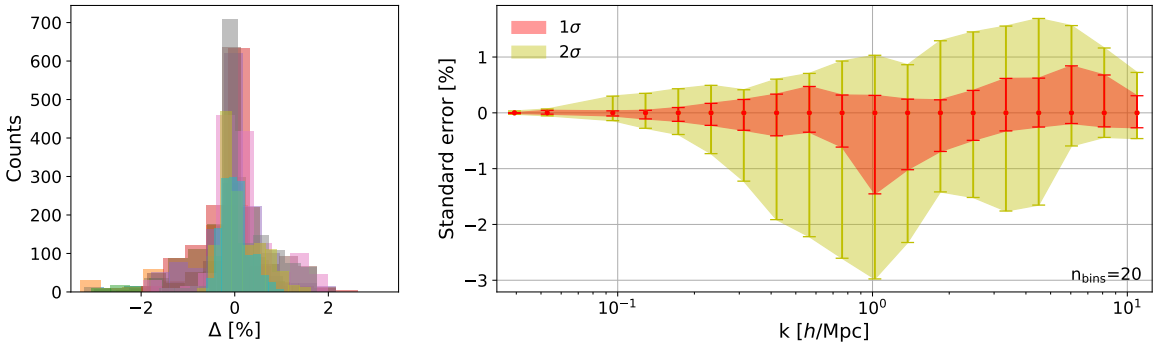

Figure 4. *Left*: histograms of the emulation errors $\Delta = \mathrm{P_{emu}}/\mathrm{P_{true}} - 1$ for each k-bin between $z = 0$ and 2. Different colours correspond to different k-bins. *Right*: 1-σ and 2-σ errors of the emulator as a function of k-modes.

emulated (dashed line) power suppression of the matter power spectrum, whereas the lower part represents the deviations between the two, i.e. the emulation error. While the emulator is very precise at sample point 1 it shows some small deviations at sample point 0, which, however, stay below ~ 3 percent at all k-modes. The other test sample points show a similar behaviour (see Fig. 13).

In order to study the accuracy of the emulator in a more quantitative way, we follow the approach presented in Fig. 4. Using the test-set with six sample points at 9 different redshift values, we study the error distribution as a function of k-modes (assuming 20 logarithmically spaced k-bins). The distribution of the relative error $\Delta = \mathrm{P_{emu}}/\mathrm{P_{true}} - 1$ is plotted in the left-hand panel of Fig. 4, where the different colours refer to the different k-bins. Based on these distributions, we define 1-σ and 2-σ errors that are plotted as a function of k-modes in the right-hand panel of Fig. 4. Not surprisingly, the emulator works best at small values of k. The poorest performance is reached on scales around $k = 1$ Mpc/h, while the precision improves again towards the smallest scales. In total the error of the emulator remains within 1.5 percent at the 1σ and within 3 percent at 2σ confidence level.

3 Weak-lensing predictions and mock observations

In this section, we describe both our prediction pipeline of the weak-lensing angular power spectrum and the construction of our mock observations. We thereby provide information on the modelling of matter power spectrum, the tomographic binning, the map generation, and the construction of the covariance matrix.

3.1 Predicting the tomographic shear power spectrum

The prediction of the tomographic cosmic shear power spectrum is based on the Limber approximation [49]. This means that the spherical harmonics power spectra are calculated via the integral

$$C_{ij}(\ell) = \int_0^{\chi_H} \frac{g_i(\chi) g_j(\chi)}{\chi^2} P_{\mathrm{dmb}}\left(\frac{\ell}{\chi}, z(\chi)\right) d\chi, \tag{3.1}$$

where the co-moving distance χ goes from 0 to the horizon χ_H. The lensing weights g_i are given by

$$g_i(\chi) = \frac{3\Omega_m}{2}\left(\frac{H_0}{c}\right)^2 \frac{\chi}{a}\int_{\chi(z)}^{\chi_H} n_i(z)\frac{\chi(z')-\chi(z)}{\chi(z')}dz', \tag{3.2}$$

and $n_i(z)$ stands for the galaxy distribution at redshift-bin i. For the full galaxy distribution, we assume

$$n(z) \propto z^2 \exp(-z/0.24) \tag{3.3}$$

which is a reasonable functional form for future galaxy survey such as Euclid. In our analysis, we assume three redshift bins between $z = 0.1$ and 1.5 with sharp bin-edges and equal galaxy counts, leading to the bin-sizes $\Delta z_1 = [0.1, 0.478]$, $\Delta z_2 = [0.478, 0.785]$, and $\Delta z_3 = [0.785, 1.5]$.

In order to mimic the effect of intrinsic alignment, we furthermore include the *nonlinear linear alignment model* of Ref. [50, 51]. The model accounts for intrinsic-intrinsic and intrinsic-shear correlations by adding one free model parameter $A_{\rm IA}$ describing the amplitude of the effect. For simplicity and in accordance with previous work [e.g. Refs. 37, 52], we ignore potential redshift and luminosity dependence of the model.

The nonlinear baryon-corrected power spectrum appearing in Eq. (3.1) is given by

$$P_{\rm dmb}(k,z) = P_{\rm dmo}(k,z) \times S_{\rm BCM}(k,z), \tag{3.4}$$

where $S_{\rm BCM}$ is the emulated baryonic suppression term defined in Eq. (2.8) and $P_{\rm dmo}(k,z)$ is the nonlinear dark-matter-only power spectrum. For the latter, we use the revised `halofit` model of Takahashi et al. [5]. The underlying transfer function is based on the Eisenstein and Hu [53] fitting function.

The revised `halofit` procedure has an accuracy of about five percent compared to high-resolution N-body simulations [3, 5]. Note that this will not be sufficient for future weak-lensing surveys such as Euclid or LSST, where more elaborate emulators will have to be used [see e.g. Ref. 10]. However, the approach is sufficient for a forecast study, especially since we use the same method for the predictions and the mock data set, thereby eliminating all systematic biases introduced by the `halofit` method.

The calculations of the auto and cross angular power spectra including the weak-lensing and the intrinsic alignment contributions are performed using the python package `PyCosmo` of Refregier et al. [54]. `PyCosmo` applies efficient numerical integration routines, allowing to obtain fast predictions necessary for high-dimensional parameter inference.

In Fig. 5 we plot the resulting angular power spectra of the cosmic shear. The 3 diagonal panels refer to the auto spectra, whereas the off-diagonal ones show the cross-spectra of the three tomographic bins. The coloured lines correspond to the predictions assuming a default cosmology from `Planck` and baryonic parameters varying within the ranges $\log M_c = [13, 16]$, $\mu = [0.1, 0.7]$ and $\theta_{\rm ej} = [2, 8]$. This corresponds to the prior ranges given in Table 2 of Sec. 4. The black data points of Fig. 5 show the Euclid-like mock observations which we will discuss in the following section.

3.2 Mock observations and covariance matrix

We build weak-lensing convergence maps based on simulated light-cones in order to construct realistic mock observations of a Euclid-like survey. The light-cones are generated from N-body simulations presented in Weiss et al. [30] that have been run using the gravity-only

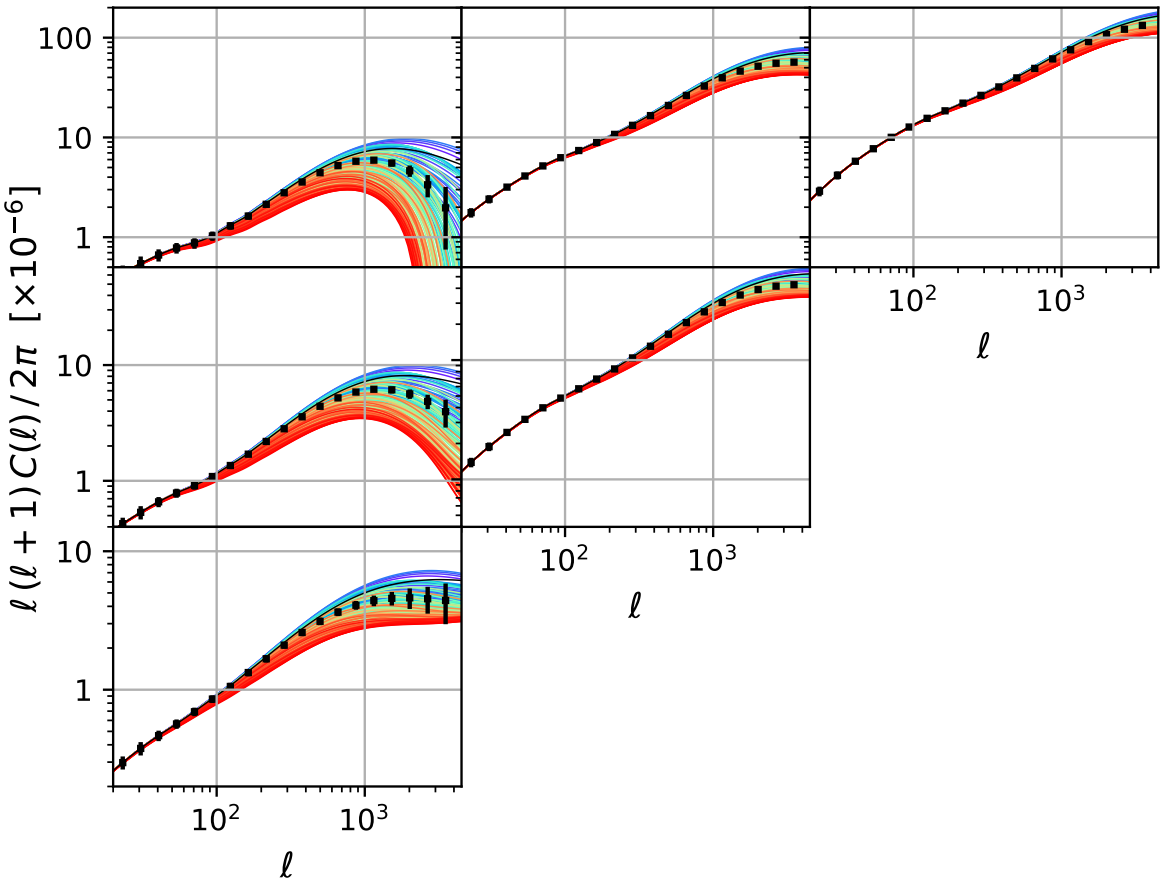

Figure 5. Mock auto and cross power spectra of the three redshift bins with error-bars that include both cosmic variance and Gaussian shape noise expected from a Euclid-like survey (black data points). The auto spectra are shown by the diagonal, the cross-spectra by the off-diagonal panels (with increasing redshift from bottom-left to top-right). The coloured lines correspond to the theoretical predictions assuming baryonic parameters $\log M_c = 13 - 16$ (mass in $M_\odot$/h), $\mu = 0.1 - 0.7$ and $\theta_{\rm ej} = 2 - 8$. The range covered by the lines illustrates the current level of uncertainty due to the baryonic effects.

N-body code `Pkdgrav3` [45, 46]. The initial conditions were created with the `MUSIC` code [55] assuming an Eisenstein and Hu [53] transfer function with a standard Planck cosmology [56].

Each simulation contains $N = 512^3$ particles and has a box-length of $L = 512$ Mpc/h. The simulation boxes are replicated up to 1728 times to obtain a full-sky light-cone between redshift $z = 0.1 - 1.5$. During the replication process, all boxes are randomly shifted and rotated. The light-cone is constructed using 78 concentric shells at different redshifts. The setup used here allows for an accuracy of about five percent in terms of the angular power spectra [30]. While this level of accuracy is not quite sufficient for stage-IV weak lensing surveys [see e.g. Ref. 3], it is good enough for the forecast purpose of this paper.

For the weak-lensing map construction, we project each shell onto a HEALPix[5] map (of $N_{\rm side} = 2048$ resolution) and weight them according to the galaxy distributions of Eq. (3.3)

[5] `https://healpix.sourceforge.io`

for each of the three redshift bins defined in Sec. 3.1. The weighted HEALPix maps are then combined assuming the Born approximation. This leads to tomographic full-sky maps of the weak-lensing convergence.

In order to obtain realistic mock observations of a stage-IV survey, we cut out a galaxy footprint of 20000 deg^2 and add a Gaussian noise component of

$$\langle \sigma^2 \rangle = \frac{\sigma_e^2}{A_{\rm pix} n_{\rm gal}} \tag{3.5}$$

to the map, where $\sigma_e = 0.3$ is the root-mean-square of the shear ellipticity dispersion, $n_{\rm gal} = 10$ arcmin^{-2} is the galaxy density for each redshift bin (summing up to a total of 30 arcmin^{-2} over the full redshift range), and $A_{\rm pix}$ is the area of a single pixel of the map. More details about the N-body simulations, the light-cone, and the convergence maps (including potential systematics) can be found in Weiss et al. [30].

In total, we rely on ten N-body simulations with different random seeds. During the light-cone construction, we furthermore apply the replication process in five different ways, which means that we are left with 50 independent light cones. Each of these full-sky light cones can account for two survey footprints leading to 100 statistically independent maps. For every map we finally assume three different noise configurations ending up with 300 different maps for every redshift bin.

We create two different mock observations one for the dark-matter-only case and one including baryonic corrections. The latter is constructed by applying the baryonification method on each of the ten N-body simulations at every output in redshift. We assume the baryon parameters $\log M_c = 13.8$ in $\mathrm{M}_\odot/\mathrm{h}$, $\mu = 0.21$, $\theta_{\rm ej} = 4$, $\eta_{\rm star} = 0.32$, and $\eta_{\rm sga} = 0.6$, which corresponds to the benchmark model B of Schneider et al. [1] and consists of a realistic model that agrees both with X-ray observations and hydrodynamical simulations.

The covariance matrix of the tomographic shear auto and cross power spectra is defined as

$$\mathrm{cov}\left[C_{ij}(\ell), C_{ij}(\ell')\right] = \left\langle \left(C_{ij}(\ell) - \langle C_{ij}(\ell)\rangle\right)\left(C_{ij}(\ell') - \langle C_{ij}(\ell')\rangle\right)\right\rangle, \tag{3.6}$$

where $\langle ... \rangle$ represents the average over all independent weak-lensing maps. The angular power spectra for the redshift bins i and j are given by $C_{ij}(\ell)$, where $i = j$ corresponds to the auto and $i \neq j$ to the cross power spectra. The variable ℓ describing the angular scale has to be discretised in bins. For illustration purposes, it is often more convenient to define the correlation matrix

$$\mathrm{corr}\left[C_{ij}(\ell), C_{ij}(\ell')\right] = \frac{\mathrm{cov}\left[C_{ij}(\ell), C_{ij}(\ell')\right]}{\sqrt{\mathrm{cov}\left[C_{ij}(\ell), C_{ij}(\ell)\right]\mathrm{cov}\left[C_{ij}(\ell'), C_{ij}(\ell')\right]}}, \tag{3.7}$$

which is nothing else than the covariance matrix normalised to its diagonal values.

We construct the covariance matrix based on the 300 baryonified and dark-matter-only weak-lensing maps at each of the three redshift bins. Individual angular power spectra are calculated using the routine anafast of the HEALPix software package. We thereby define 19 ℓ-bins going from $\ell = 20$ to 4000. The bins are equally separated in logarithmic space.

In Fig. 6 we plot the correlation matrices obtained from both the dark-matter-only (left) and the baryon-corrected maps (right). They include the three auto (11, 22, 33) and three cross correlation terms (12, 13, 23) for all 19 ℓ-bins. The top-panels show the correlation matrices without shape noise. They illustrate the well-known fact that small-scale modes are correlated, which is a direct consequence of the non-linear nature of structure formation. The

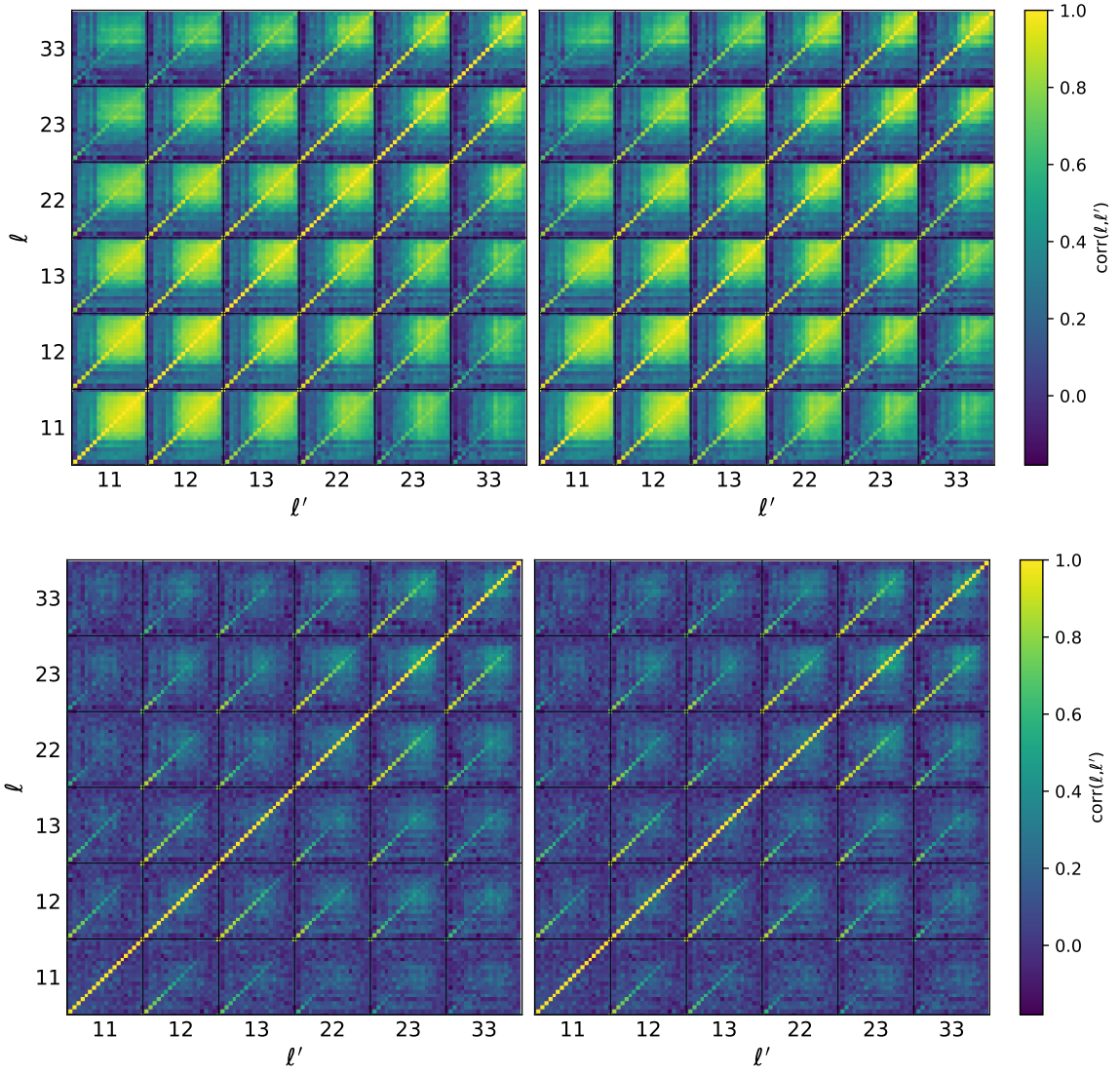

Figure 6. Normalised covariance matrices of the tomographic cosmic shear power spectrum without and with baryonic effects (left and right). For the baryonic effects, we assume a realistic model that has been shown in S19 to agree well with X-ray observations (see benchmark model B-avrg in S19 [1]). The top-panels are noise free, whereas the bottom panels include Gaussian shape noise expected for a Euclid-like survey (see text).

bottom-panels, on the other hand, show the full correlation matrices including shape-noise errors. The latter strongly suppress any correlations, leading to subdominant off-diagonal terms over all scales. A closer look at Fig. 6 reveals that the differences between dark-matter-only and baryon-corrected covariances remain very small. This is not only true for the full covariance matrix but also for the noise-free case where potential deviations should be more visible.

Finally, with the covariance matrix at hand, we can build our mock observations. In principle this would be possible using the spherical harmonic auto and cross power spectra directly measured on our simulations. However, the maps suffer from a few-percent power

Parameter description	Acronym	True value	Prior range
Cosmic baryon abundance	Ω_b	0.049	$0.04 - 0.06$
Cosmic matter abundance	Ω_m	0.315	$0.15 - 0.42$
Clustering amplitude	σ_8	0.811	$0.66 - 0.9$
Spectral index	n_s	0.966	$0.9 - 1.0$
Reduced Hubble parameter	h_0	0.673	$0.6 - 0.9$
Baryonic parameter 1 (related to slope of gas profile)	$\log M_c$	13.8	$13 - 16$
Baryonic parameter 2 (related to slope of gas profile)	μ	0.21	$0.1 - 0.7$
Baryonic parameter 3 (related to maximum gas ejection)	$\theta_{\rm ej}$	4	$2 - 8$
Amplitude of intrinsic alignment	$A_{\rm IA}$	1	$0 - 2$

Table 2. Parameter descriptions, acronyms, true value (used in the mock data set), and prior ranges for the cosmological, baryonic, and intrinsic alignment parameters. All priors are assumed to be flat.

depletion at the largest scales due to the limited box size and the randomisation procedure [see also Ref. 30]. Furthermore, we use the revised `halofit` framework of Takahashi et al. [5] for the predictions. The latter is only about 5 percent accurate in the non-linear regime, leading to a shift in the posterior, which becomes visible when stage-IV lensing survey configuration are assumed. We therefore only use the simulated maps for the covariance matrix and directly use the revised `halofit` results for the mock angular power spectrum. Note, however, that this is primarily an aesthetic choice which does not affect the conclusions of the paper.

The resulting mock power spectra are plotted as black symbols in Fig. 5. The error bars correspond to the (square-root of the) diagonal values of the covariance matrix and are the result of our light-cone simulations and weak-lensing map generation procedure. They consist of a combination of Gaussian noise and statistical errors assuming a Euclid-like galaxy resolution and survey footprint. The default cosmological, baryonic, and intrinsic alignment parameters used for the mock data are summarised in Table. 2.

4 Parameter forecast analysis

Based on the mock angular power spectrum shown in Fig. 5, we now perform a number of likelihood analyses to estimate the constraining power of a stage-IV weak lensing survey, assuming a standard ΛCDM cosmology. This means we simultaneously vary five cosmological parameters (Ω_b, Ω_m, σ_8, n_s, h_0), one intrinsic-alignment parameter ($A_{\rm IA}$), and three gas parameters (M_c, μ, $\theta_{\rm ej}$). The remaining baryonic parameters describing the stellar components ($\eta_{\rm star}$, $\eta_{\rm cga}$) are kept fixed for simplicity. This choice can be justified by the fact that the stellar components are relatively well known and have a comparable minor effect on the power spectrum (see Fig. 2 in S19). However, we explicitly investigate the role of stellar parameters in Appendix B, showing that they have no noticeable effects on cosmological parameter estimates of stage-IV weak lensing surveys.

All model parameters including their prior ranges are summarised in Table 2. The priors on the cosmological and intrinsic-alignment parameters are selected to be wide enough to not affect the posteriors. Only the baryon-abundance Ω_b, which is not very sensitive to the weak-lensing signal, has been set to a range motivated by (but significantly broader than) results from the CMB [57] and nucleosynthesis [e.g. Ref. 58]. The priors on the baryonic parameters are selected so that they comfortably include the predictions of all known hydrodynamical simulations. This can be verified in Fig. 1 where the grey area indicates the resulting spread in the matter power spectrum for modifications of baryonic parameters within the above prior

ranges. In the following we will see that the priors on M_c and $\theta_{\rm ej}$ are wide enough so that these parameters are uniquely constrained by the weak-lensing shear power spectrum. This is not the case for the third parameter μ, which, however, has a much weaker effect on the cosmological signal. All priors are assumed to be flat.

4.1 Cosmological parameters

The goal of this section is to investigate and compare different strategies for dealing with baryonic effects on the tomographic weak-lensing shear power spectrum. This allows us to assess potential biases from simplifying assumptions. The strategies are the following:

(i) First, we consider the case where baryonic effects are completely ignored in the prediction pipeline. Although we know this assumption to be inaccurate, we want to quantify the introduced bias on the cosmological parameters.

(ii) Second, we ignore baryonic effects but consider only data from the largest cosmological scales with $\ell \leq 100$ (where baryonic effects are subdominant). While this should reduce the biases on cosmological parameters, it will also increase the size of their contours.

(iii) As a third step, we carry out a parameter inference analysis including baryons in the prediction pipeline and and marginalising over all baryonic parameters to determine the cosmology. This should give us a realistic estimate of the expected accuracy from the weak-lensing shear power spectrum alone (assuming a Euclid-like survey).

(iv) Finally, we perform the same exercise, however, this time keeping all baryonic parameters at a fixed value. This corresponds to an ideal situation where baryonic parameters are perfectly determined with external data from gas observations.

For each of these four cases, we run a cosmological inference sampling and we analyse the size of the resulting parameter contours as well as potential biases with respect to the true cosmology of the mock data set. The inference is performed using the Markov-Chain Monte Carlo (MCMC) sampler `UHAMMER` [59] which is based on the `emcee` code [60].

Fig. 7 highlights the results for the cosmological parameters (Ω_m, Ω_b, σ_8, h_0, and n_s) while the baryonic and intrinsic-alignment parameters are marginalised over. Scenario (i) of the above list is shown in black, illustrating what happens if the baryonic effects are ignored in the analysis pipeline. While the resulting contours are very tight, they are strongly biased with respect to the true cosmology. Depending on the cosmological parameter, the bias is typically between about 5 and 10 standard deviations. This is a much stronger effect than in original work [61, 62] but in qualitative agreement with more recent findings from Refs. [24, 63] that included the effects of AGN feedback. We conclude that ignoring baryonic effects would lead to very wrong conclusions about cosmology.

The grey contours represent the scenario (ii), where all scales significantly affected by baryons are ignored. According to Fig. 5, this requires a cut at $\ell = 100$, which means that only about one third of the available data points are used in the MCMC analysis. While such a strategy of cutting small-scale information does not lead to a noticeable bias (the grey contours are well centred around the true cosmology indicated by the black cross), the constraining power remains poor for all parameters.

The red contours of Fig. 7 illustrate the scenario (iii), where all scales are included in the analysis and baryonic effects are modelled according to the baryonic correction model of Sec. 2. The baryonic model parameters are allowed to vary freely within the prior ranges provided

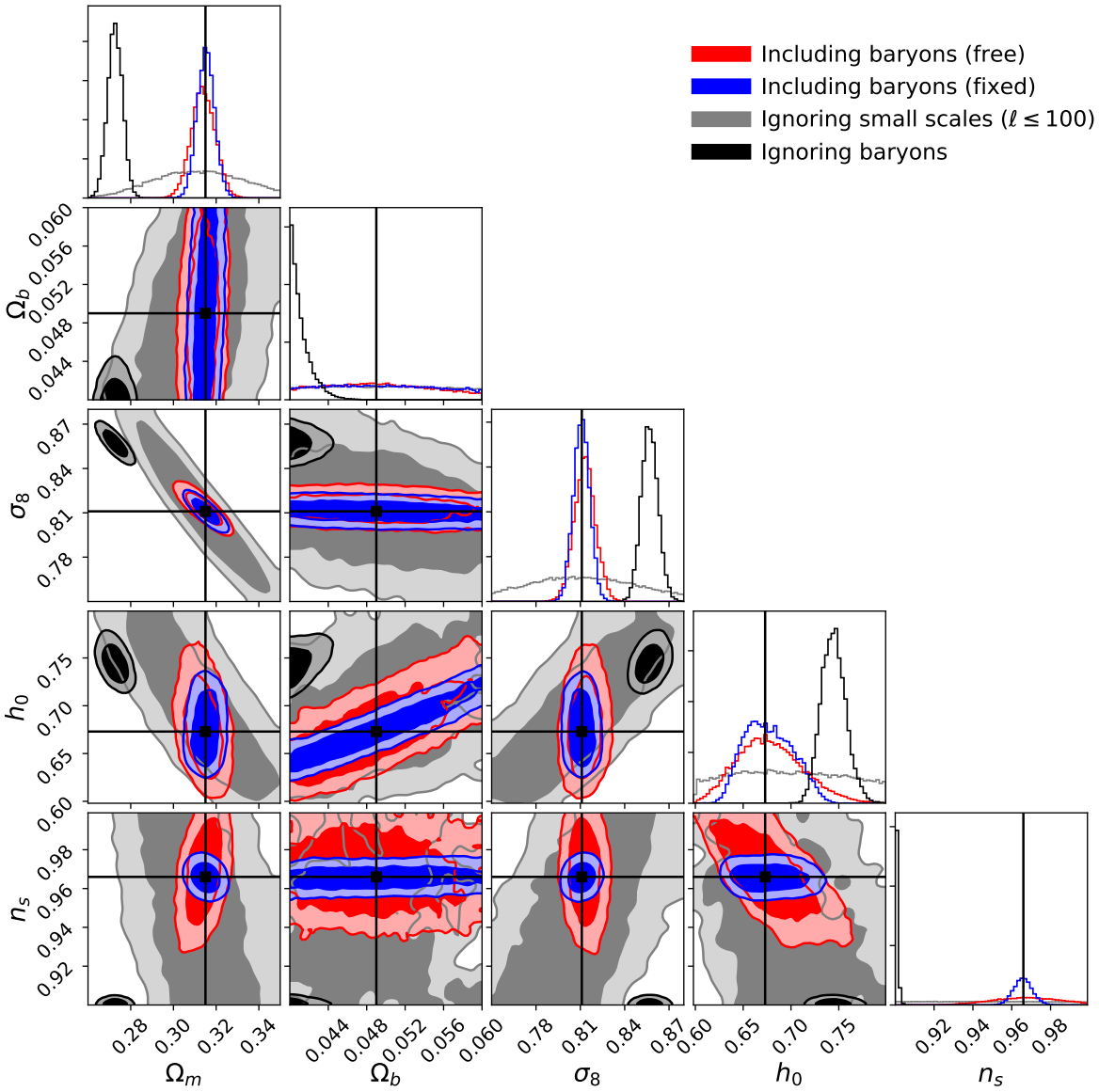

Figure 7. Posterior contours of all cosmological parameters assuming a Euclid-like setup for the cases when baryonic effects are either included (red, blue) or ignored (black, grey). The true parameter values of the mock data are indicated by black lines. Ignoring baryonic effects leads to strong biases (black) except if small scales are ignored (grey). Accounting for baryonic effects while including all scales (up to $\ell = 4000$) makes the posterior contours shrink significantly, especially if the baryonic parameters are fixed (blue) instead of marginalised over (red).

in Table 2. They are marginalised over together with the intrinsic-alignment parameter. The resulting constraints on Ω_m and σ_8 are each about a factor of four tighter than the contours from large-scales only. This highlights the importance of including small scales in the analysis of future weak-lensing observations. Other parameters such as Ω_b and n_s remain rather poorly constrained.

Finally, the blue contours of Fig. 7 illustrate the scenario (iv), where baryonic parameters are fixed to their correct values. This corresponds to the ideal situation where all baryonic

effects are fully determined. Compared to the case where baryonic effects are marginalised over, the error on n_s shrink by more than a factor of 2, while the errors on h_0, σ_8, and Ω_m shrink by bout 50 percent or less. While this is a noteworthy improvement, it also tells us that weak-lensing shear alone (without additional data from gas observations) results in surprisingly tight constraints of cosmological parameters. It is unclear whether this will also be the case for extensions of the cosmological model, which could affect the power spectrum in ways that are degenerate with the baryonic effects.

The posterior contours shown in Fig. 7 make it very clear that future weak lensing surveys such as Euclid or LSST require a proper parametrisation of baryonic effects. In terms of the key cosmological parameters Ω_m and σ_8, parametrising and marginalising over baryonic parameters leads to more than 3 snd 5 times tighter error bars compared to the conservative case where only modes that are unaffected by baryons are considered. In terms of the contour area, which is often used as a measure of the Figure of Merit, the improvement is more than a factor of 15.

The above analysis also shows that external prior information on the baryonic parameters has the potential to further reduce the errors on cosmological parameters. However, for Ω_m and σ_8, the improvement on the individual errors is about 50 percent at best, for the contour area it is not more than a factor of two. This is a noticeable, but not a dramatic improvement. However, it is possible that adding gas information becomes more important when investigating extensions of the minimal cosmological model. In Paper II [32], we will combine the angular power spectra with mock data of X-ray gas fractions and we will investigate the models including massive neutrinos and extensions of the ΛCDM model.

4.2 Baryonic parameters

We now turn our focus towards the baryonic parameters M_c, μ, and $\theta_{\rm ej}$. They describe the gas profiles of galaxy groups and clusters (see Eq. 2.5) thereby affecting the weak-lensing signal. While the baryonic parameters are best constrained using direct gas observations, we will now investigate whether weak-lensing shear data alone can constrain baryonic feedback parameters as well.

Fig. 8 shows the posterior contours of the baryonic parameters together with the Ω_m and σ_8 parameters. The values of the parameters assumed for the mock data are indicated with black lines (they correspond to the beat-fitting values from current X-ray data, see S19). The red and blue contours correspond to the scenarios (iii) and (iv) from the previous section. The latter does only appear in the top panel, since for this case all baryonic parameters are fixed to their true values. Fig. 8 shows that both the M_c and $\theta_{\rm ej}$ parameters (describing the slope of the maximum extend of the gas profile) are constrained well beyond the original prior-range. The third parameter μ, on the other hand, shows a rather flat posterior distribution over the full prior range. This is not surprising, since μ has been shown in S19 [1] to be the least sensitive of the baryonic parameters regarding changes of the matter power spectrum.

In summary, Fig. 8 shows that future weak-lensing data will be able to not only constrain cosmology but astrophysical effects such as gas ejection from AGN feedback and its dependence on halo mass. Note, however, that with additional data from gas observations it will be possible to pin down baryonic parameters at much higher precision. In Paper II [32] we will show this using gas fractions from the upcoming X-ray survey eROSITA.

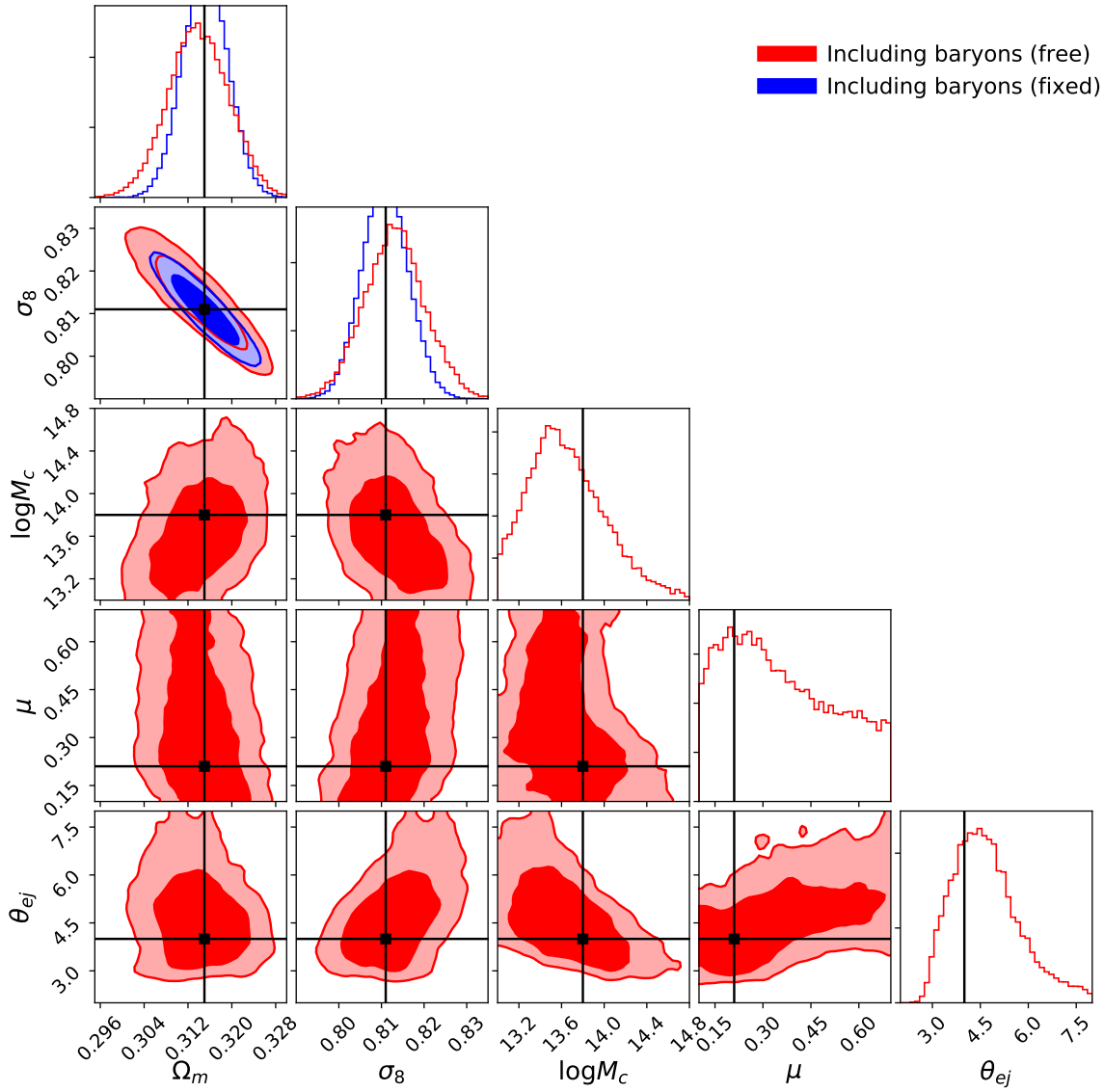

Figure 8. Posterior contours of the baryonic parameters $\log M_c$, μ, and $\theta_{\rm ej}$ together with Ω_m and σ_8. All other cosmological and intrinsic-alignment parameters are marginalised over. The red and blue contours correspond to the cases (iii) and (iv) in the text, where the three baryonic parameters are either left free to vary or fixed to the values assumed in the mock (indicated by black lines). The red contours show that a Euclid-like shear power spectrum alone is able to put limits on the parameters $\log M_c$ and $\theta_{\rm ej}$ while μ remains largely unconstrained. Additional observations from X-ray will be able put much more stringent limits on baryonic parameters (see Paper II [32]).

4.3 Allowing for additional freedom in the redshift evolution

The baryonic correction (BC) model does not account for any explicit redshift dependence of the gas, stellar, or dark-matter density profiles. The apparent redshift-evolution of the power spectrum (visible for example in Fig. 3) is a result of the fact that at different redshift the signal is dominated by haloes of different mass. Although this implicit redshift evolution is in good agreement with some hydrodynamical simulations, the true redshift evolution of the

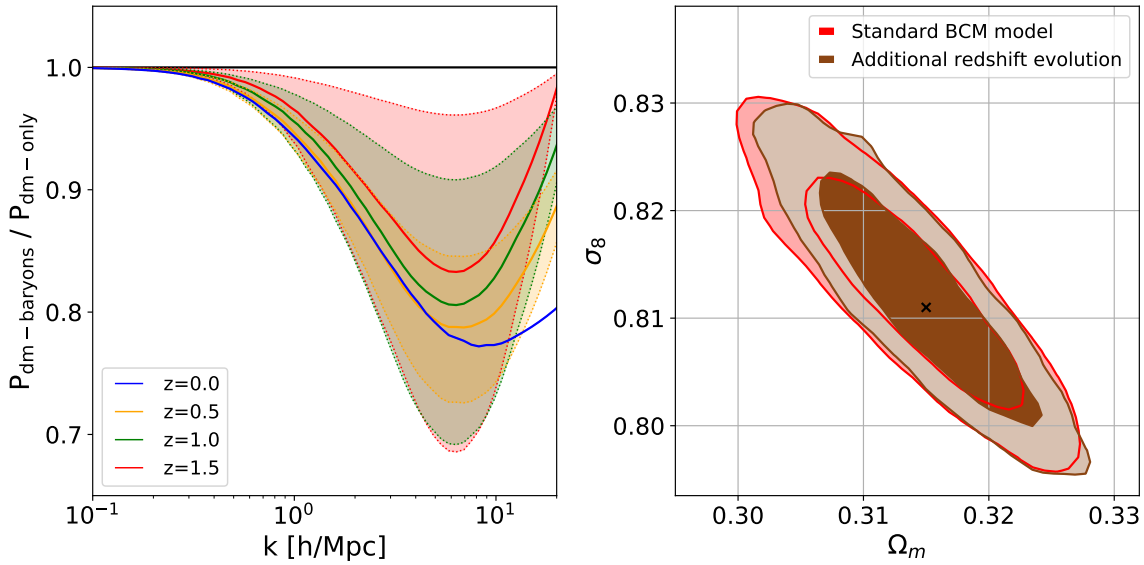

Figure 9. Effects of an additional free parameter (γ) quantifying deviations from the standard redshift evolution of the baryonic suppression signal. *Left:* Baryonic suppression on the matter power spectrum for a `Planck` cosmology and default baryonic parameters. The coloured solid lines show the original redshift evolution of the BC model, the shaded regions (delimited by dotted lines) indicate the additional freedom provided by the γ-parameter of Eq. (4.1) assuming a prior range of $\gamma \in [-0.5, 0.5]$. *Right:* resulting posterior contours (at 0.68 and 0.95 confidence level) of the original case (red) and the case with additional marginalised redshift parameter γ. We have checked that the agreement between the two cases is similar for the remaining parameters.

baryonic suppression effect remains uncertain [see S19 1].

In this section, we investigate whether further freedom in the redshift evolution has a significant effect on the posterior contours of cosmological parameters. We therefore introduce an explicit redshift parameter at the level of the matter power spectrum. This is done by replacing the baryonic suppression signal (defined in Eq. 2.8) with the relation

$$S_{\rm BCM}(k,z) \;\rightarrow\; S_{\rm BCM}(k,z) + [1 - S_{\rm BCM}(k,z)^{\gamma z}] \tag{4.1}$$

in Eq. (3.4). The new parameter γ is allowed to vary freely within the prior ranges $\gamma = [-0.5, 0.5]$. If $\gamma > 0$ ($\gamma < 0$), the baryonic suppression gets reduced (increased) towards higher redshifts, whereas $\gamma = 0$ means no change with respect to the previous model.

Note that the above redshift evolution does not allow for the same amount of freedom as adding explicit redshift dependencies into the gas, stellar, and dark matter profiles of the BC model (defined in Sec. 2.1). However, we have checked that Eq. (4.1) allows us to mimic the redshift evolution of hydrodynamical simulations to reasonable precision. The redshift dependency of the Cosmo-OWLS runs, for example, can be reproduced at the 2 percent level up to $k \sim 7$ h/Mpc with $\gamma = 0.17$. Similar or better agreement is found for the OWLS, Horizon-AGN, and Illustris-TNG simulations.

In the left panel of Fig. 9, we illustrate the effect of the additional γ-parameter on the relative power spectrum ($S_{\rm BCM}$). At each redshift, the shaded region shows the additional freedom of $S_{\rm BCM}$ if γ is varied within the prior ranges between $\gamma = -0.5$ (lower limit) and

$\gamma = 0.5$ (upper limit). The solid lines in the centre of the shaded regions indicate the case of $\gamma = 0$. The added variability due to the additional redshift parameter grows from zero at $z = 0$ to nearly the size of the baryon suppression signal at $z = 1.5$.

The right panel of Fig. 9 shows the Ω_8-σ_8 contours resulting from MCMC chain including all parameters of Table 2 plus the additional redshift parameter γ (brown).The contour shows no significant change in size compared to the standard case with fixed $\gamma = 0$ (red). We have checked that this is also the case for the remaining parameter contours not shown in this plot.

Based on Fig. 9 we conclude that, although the BC model might not be general enough to include the full range of potential redshift dependence, such an effect is unlikely to significantly affect cosmological parameter estimates. This confirms the validity of the results shown in the present paper.

4.4 Potential biases from the estimated covariance

Before we move on and investigate possible simplifications of the baryonification method, let us discuss the potential presence of biases caused by our estimate of the covariance matrix. It has been argued by Hartlap et al. [64] that, in order to not underestimate the posterior contours, the inverse of the covariance matrix has to be corrected by the factor $\alpha = (N-p-2)/(N-1)$, where p is the length of the data vector and N is the number of realisations used to construct the covariance matrix. More recently, Sellentin and Heavens [65] showed that correcting for the uncertainties in the covariance matrix furthermore requires the Gaussian likelihood to be replaced by a multivariate t-distribution.

Note that all posterior contours from this paper have been estimated using a Gaussian likelihood without recalibrating the covariance matrix. In order to test the validity of this approach, we have performed an additional MCMC run based on the prescription of Sellentin and Heavens [65] (i.e. replacing the multivariate Gaussian by a t-distribution and adding the pre-factor α to the inverse of the covariance matrix). As a result, we found posterior contours that are effectively indistinguishable compared to the ones from the uncorrected analysis. We therefore conclude that our results are unlikely to be plagued by significant biases related to the construction of the covariance matrix.

5 Testing simplifying model assumptions

Current weak-lensing studies generally rely on simplifying assumptions for baryonic effects in their analysis pipeline. For example, baryonic effects are usually not included in the covariance matrix and any potential cosmology dependence of baryonic parameters is ignored. In this section, we evaluate whether it will be acceptable to ignore these effects in the analysis pipeline of future weak-lensing surveys such as Euclid or LSST.

5.1 Cosmology dependence of the baryonic suppression

In the first part of this paper, we have established that the baryonic suppression of the power spectrum is sensitive to the mean baryon fraction $f_b = \Omega_b/\Omega_m$. While this dependency is fully accounted for in our analysis, this is not the case for other studies where any cosmology dependence of baryonic effects is usually ignored. We now investigate whether this simplifying assumption has any effect on cosmological parameter estimates.

The test is performed by comparing the posterior contours of the full analysis with a test-case where the baryonic fraction $f_b = \Omega_b/\Omega_m$ of Eq. (2.7) is fixed to the Planck-value of $f_b = 0.155$. This means that while gravitational clustering remains sensitive to variations

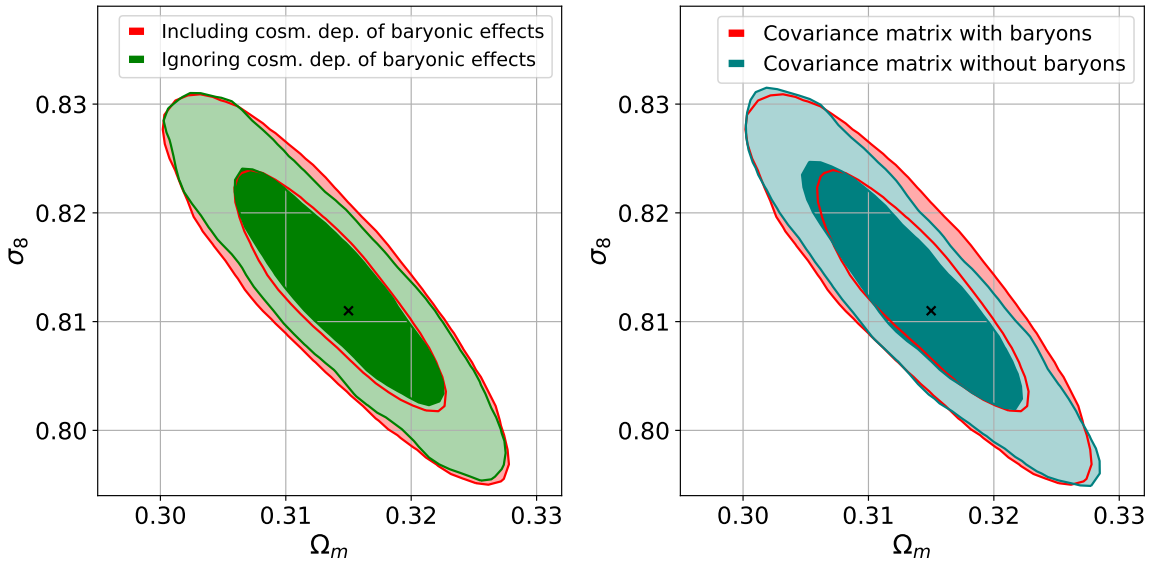

Figure 10. Investigating the effects of simplifying assumptions of baryonic modelling on the cosmological parameters Ω_m and σ_8. *Left:* Change of the posterior contours if the cosmology dependence between baryonic and cosmological parameters is ignored (green) instead of being properly included (red). The former is obtained by fixing the cosmic baryon fraction to $f_b = 0.155$ in the BC model during the MCMC run. *Right:* Change of the posterior contours if the baryons are ignored in the covariance matrix (steal-blue) instead of being included (red). We have checked that the level of agreement between the contours is similar for the other cosmological parameters.

of Ω_b and Ω_m, the baryonic suppression effect ($S_{\rm BCM}$) becomes completely decoupled from cosmology. In the left panel of Fig. 10 we compare the Ω_m-σ_8 contours from a BC model with fixed f_b (green) to the generic case with fully cosmology-dependent baryonic parameters (red). Both contours are very similar, showing no significant bias in the Ω_m-σ_8 plane. We have checked that the same is true for the contours of all other parameters.

In order to investigate potential biases due to the selected value of f_b, we perform the same test assuming baryonic fractions of $f_b = 0.13$ and $f_b = 0.18$, respectively. Note that these values differ from the assumed cosmology of the mock data sample. As a result, we find a visible but very small shift of the Ω_m-σ_8 contours towards the bottom-right corner for increasing f_b. However, the shift remains much smaller than the estimated posterior contours for reasonable values of f_b.

The results presented in the left panel of Fig. 10 retrospectively validate the assumptions made in weak-lensing analysis by KiDS [37], DES [38], and HSC [39], where parametrised baryonic suppression functions were multiplied to the power spectrum without considering any cosmology dependence. Furthermore, the results show that ignoring cosmology dependence of baryonic effects also consist of an acceptable strategy for for future, stage-IV weak lensing surveys. It remains to be checked if these conclusions are also valid for other measures beyond the two-point statistic.

5.2 Baryonic effects on the Covariance matrix

In Sec. 3.2, we have calculated the covariance matrix of the tomographic shear power spectrum with and without baryonic suppression effects. The goal of the current section is to establish, if it is sufficient to only account for baryonic effects at the level of the power spectrum or if they also have to be included in the covariance matrix. Note that we only compare the two cases of a dark-matter-only and a fixed baryonified covariance matrix (assuming the benchmark model B-avrg, see S19) and we do not vary the baryonic parameters during the parameter inference.

The right-hand panel of Fig. 10 illustrates the Ω_m-σ_8 contours when baryons are ignored (steel blue) and included (red) in the covariance matrix. Both contour areas are very similar in size and they show no noticeable offset with respect to each other. Although Fig. 10 only illustrates the Ω_m-σ_8 contours, we have checked that this is also true for all other parameters.

Based on the findings of the section, we conclude that for future stage-IV weak-lensing surveys, it will be sufficient to calculate the covariance matrix of the cosmic shear power spectrum using gravity-only N-body simulations. This considerably simplifies the analysis pipeline of stage-IV weak-lensing surveys.

5.3 Reducing the number of baryonic parameters

The baryonic correction model introduced in S19 consists of 5 free parameters, 3 describing to the gas distribution (M_c, μ, $\theta_{\rm ej}$) and 2 related to the stellar component ($\eta_{\rm star}$, $\eta_{\rm cga}$). The same parameters (together with the cosmic baryon fraction f_b) were used to construct the baryonic emulator in Sec. 2.3. For the forecast analysis, however, we only varied the gas parameters, whereas the stellar parameters were kept constant. This can be justified by the fact that the stellar fractions are well known from observations and that they have a comparably small effect on the baryonic suppression signal. However, we explicitly show in Appendix B that adding stellar parameters to the inference sampling does not have any noticeable effect on the resulting cosmological parameter contours.

In the present section, we aim to investigate the role of the three baryonic parameters M_c, μ, $\theta_{\rm ej}$ on the cosmological parameters contours. More specifically, we want to find out if further reducing the number of free baryonic parameters has a noticeable effect on the size of the error bars. We therefore run two additional MCMC chains, one where μ is fixed while M_c, and $\theta_{\rm ej}$ are allowed to vary, and another one where μ and $\theta_{\rm ej}$ are both fixed and only M_c is allowed to vary.

The cosmological parameter contours resulting from this exercise are plotted in Fig. 11. While the red and blue contours correspond to the cases of fully varying and fully fixed baryonic parameters (already shown in Fig. 7), the magenta and cyan cases show the new results with one (μ) and two (μ, $\theta_{\rm ej}$) fixed parameters, respectively. As expected, the contours of all cosmological parameters become larger the more baryonic parameters are allowed to vary. The increase is largest when going from 0 to 1 baryonic parameter (blue to cyan). However, there is a further gradual increase of contours when going from 1 to 2 (cyan to magenta) and from 2 to 3 (magenta to red) baryonic parameters. This becomes evident, for example, in the parameter plane of Ω_m and σ_8, where for each added free parameter, the contour areas increase by about ~ 30 percent.

Based on the results of Fig. 11, we conclude that it is necessary to allow all 3 baryonic model parameters to vary in order to get an accurate estimate of the total error budget. We therefore retain the same baryonic prescription for the analysis pipeline of Paper II.

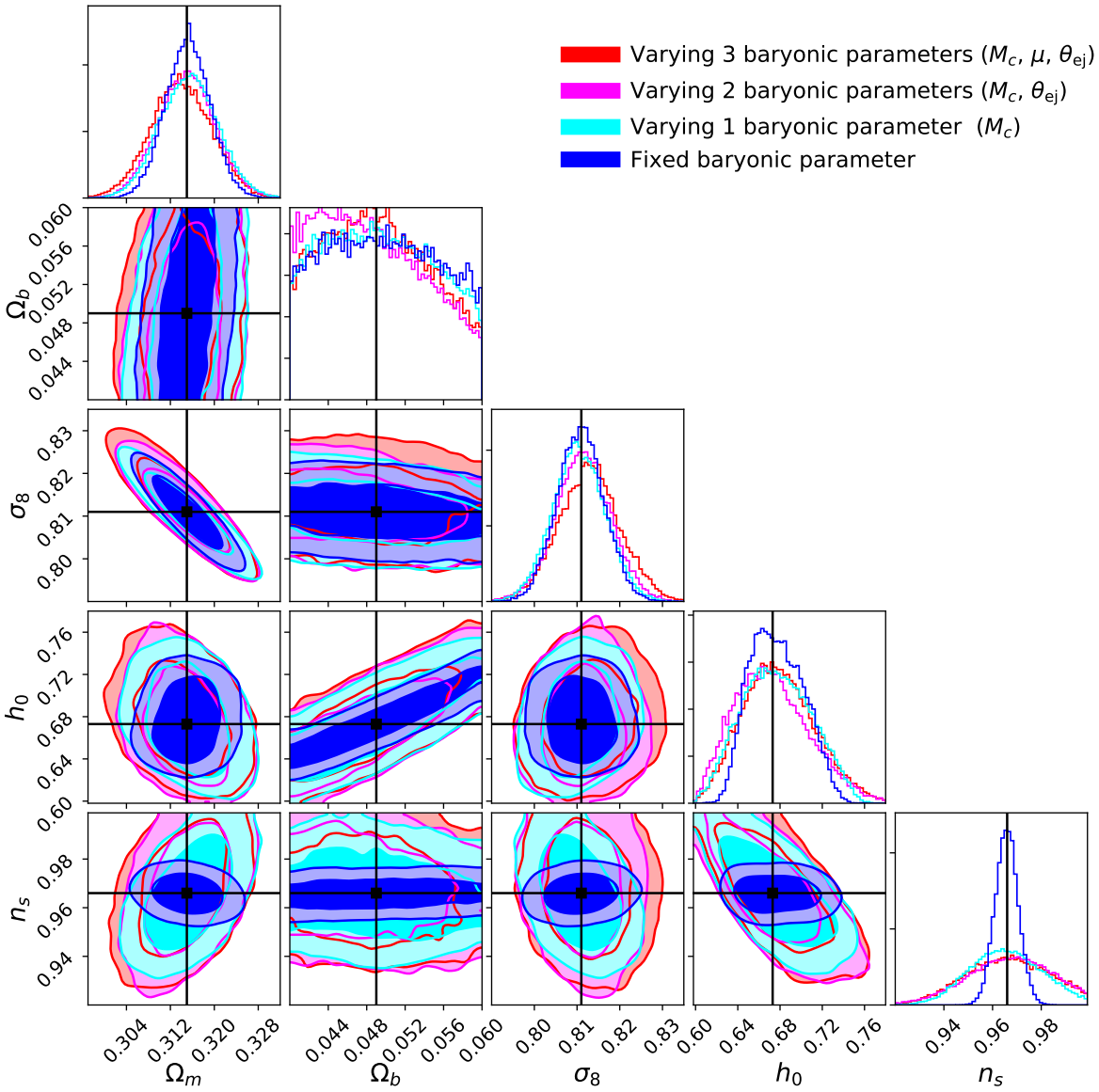

Figure 11. Change of the cosmological parameter contours when the amount of free baryonic parameters are reduced from the original 3 (red) to 0 (blue). The red and blue contours have already been shown in Fig. 7. The magenta contours correspond to the case where M_c and $\theta_{\rm ej}$ are allowed to vary while μ is fixed. The cyan contours show the case where only M_c can vary while μ and $\theta_{\rm ej}$ are fixed. The black lines indicate the true cosmology from the mock data.

6 Conclusions and outlook

Future stage-IV weak lensing surveys will be affected by baryonic processes, more particularly the redistribution of gas due to high energetic feedback effects driven by active galactic nuclei (AGN). In this paper, we carried out a forecast study investigating the effects of baryons on cosmological parameter estimates for a Euclid-like weak-lensing survey. We run a suite of simulations to construct a mock data set consisting of a tomographic shear power spectrum and a corresponding covariance matrix covering the range $\ell = 20 - 4000$. Based on this mock,

we run a MCMC chain, simultaneously varying five cosmological (Ω_m, Ω_b, σ_8, h_0, n_s), one intrinsic alignment ($A_{\rm IA}$), and three baryonic (M_c, μ, $\theta_{\rm ej}$) parameters. The resulting posterior contours are compared to other likelihood analyses, where baryonic effects are either ignored or fixed to the true value. In the following, we list the main conclusions obtained from this investigation:

- Ignoring the effects of baryons in the prediction pipeline leads to very wrong conclusions regarding cosmology. All cosmological parameters are biased by 5 standard deviations or more compared to the assumed cosmology of the mock data-set. Furthermore, ignoring baryons results in a severe underestimation of the theoretical uncertainties, leading to very tight contours and the false impression of high accuracy.

- One straight-forward way to reduce the bias without properly modelling the baryonic effects is to only include the largest cosmological modes that remain unaffected by baryonic feedback. This strategy, however, requires a cut at $\ell \lesssim 100$, which means that most of the data remains unused. While this approach indeed gets rid of the bias, it leads to strongly increased error-bars of the cosmological parameters. Regarding σ_8 and Ω_m, the 95 percent confidence levels increase by more than a factor of 3 and 5, respectively. In terms of contour areas, this corresponds to an increase of a factor of 15. Hence, ignoring all scales affected by baryons strongly reduces the constraining power of stage-IV weak lensing surveys.

- Including baryonic effects via the baryonic correction model (assuming 3 free baryonic parameters) results in tight (and unbiased) posterior contours of cosmological parameters. This is especially true for Ω_m and σ_8, whereas h_0 and n_s are less well constrainable. We also obtain constraints on the baryonic parameters themselves, which means that future shear observations can be used to learn more about feedback processes.

- Next to the strategy of including baryonic parameters and marginalising over them, we have also investigated what happens to the cosmological parameters if the baryonic parameters are fixed to their true value. This corresponds to an idealistic case where baryonic effects are fully constrained by external data (such as X-ray or SZ observations, for example). Fixing baryonic parameters leads to a $\sim 20-30$ percent reduction of errors for σ_8, Ω_m, while the improvement is about 50 percent for h_0 and a factor of 3 for n_s. However, considering that the latter two parameters are already strongly constrained by CMB observations, we conclude that parametrising baryonic effects and marginalising over the baryonic parameters leads to surprisingly strong constraints on cosmology.

- The baryonic suppression effect shows a weak dependence with the cosmological parameters Ω_b and Ω_m while other parameters are not affected. This is because the cosmic baryon fraction $f_b = \Omega_b/\Omega_m$ determines the amount of available gas that is involved in the feedback process. In terms of the baryon-induced suppression of the matter power spectrum, the amplitude of the suppression increases by about a factor of two if f_b is changed by a factor of two. However, despite this obvious link between baryonic and cosmological effects, we have shown that fixing f_b to a constant value in the BC model only leads to very small shifts of the posterior contours well below the estimated one sigma error. This means that correcting the nonlinear clustering signal in a cosmology independent way is an acceptable approximation to account for baryonic effects for a Euclid-like survey.

- We have constructed two versions of the covariance matrix one with and one without baryonic correction effects, running MCMC chains for both. We found no noticeable difference of the posterior contours between the two cases. Therefore, we conclude that, while baryonic effects play an important role in the prediction of the angular power spectrum, it is safe to neglect them in the covariance matrix.

- Finally, we have investigated what happens if the baryonic correction model with originally 3 free parameters (M_c, μ, $\theta_{\rm ej}$) is reduced to 2 parameters (M_c, $\theta_{\rm ej}$) or 1 parameter (M_c) instead. We showed that each baryonic parameter contributes to the cosmological parameter contours, justifying the use of 3 parameters to describe the baryonic effects on the weak-lensing signal.

The analysis presented here is based on the *baryonic correction model* of S19 [1], which consists of an empirical method to model baryonic effects on the large-scale density field of the universe. The model is consistent with full hydrodynamical simulations showing 2 percent agreement or better with respect to the power spectrum at redshift zero and up to $k \sim 10$ h/Mpc. Note, however, that the model currently does not assume any explicit redshift dependence of the gas profiles. Current X-ray observation and some hydrodynamical simulations are consistent with this assumption, but rather large uncertainties remain. We have run a MCMC chain where we allowed for additional freedom in the redshift dependence of the baryonic power suppression. This additional redshift parameter does not lead to significantly different posterior contours, confirming that the above results are not driven by too restricted model assumptions regarding the redshift evolution.

In a companion paper [32, Paper II] we will extend the present analysis to a more realistic cosmological model that includes massive neutrinos. Furthermore, we will investigate three straight-forward extensions to ΛCDM: a dark energy model with dynamical equation of state (wCDM), a modified gravity model based on the $f(R)$ extension of the Einstein-Hilbert action (fRCDM), and a model with a mixed dark matter sector (ΛMDM). Another goal of Paper II is to investigate how much can be gained in terms of cosmological parameter contours, if Euclid-like data from the weak-lensing shear power spectrum is combined with X-ray observations of the cluster gas fractions from the upcoming eROSITA survey.

Acknowledgments

The authors would like to thank Uwe Schmidt for computational support as well as Tomasz Kacprzak, Adam Amara, Raphael Sgier, and Federica Tarsitano for many helpful scientific discussions. This work has been supported by the Swiss National Science Foundation via the project numbers PZ00P2_161363 and PCEFP2_181157. AR wants to thank the KIPAC institute at Stanford University where part of this work has been completed. Some of the results in this paper have been derived using the healpy and HEALPix software [66]. Some of the plots rely on the `conrer.py` package [67].

References

[1] Aurel Schneider, Romain Teyssier, Joachim Stadel, Nora Elisa Chisari, Amandine M. C. Le Brun, Adam Amara, and Alexandre Refregier. Quantifying baryon effects on the matter power spectrum and the weak lensing shear correlation. *JCAP*, 1903(03):020, 2019. doi: 10.1088/1475-7516/2019/03/020.

[2] Katrin Heitmann et al. The Cosmic Code Comparison Project. *Comput. Sci. Dis.*, 1:015003, 2008. doi: 10.1088/1749-4699/1/1/015003.

[3] Aurel Schneider, Romain Teyssier, Doug Potter, Joachim Stadel, Julian Onions, Darren S. Reed, Robert E. Smith, Volker Springel, Frazer R. Pearce, and Roman Scoccimarro. Matter power spectrum and the challenge of percent accuracy. *JCAP*, 1604(04):047, 2016. doi: 10.1088/1475-7516/2016/04/047.

[4] Lehman H. Garrison, Daniel J. Eisenstein, and Philip A. Pinto. A High-Fidelity Realization of the Euclid Code Comparison N-body Simulation with Abacus. *Mon. Not. Roy. Astron. Soc.*, 485(3):3370–3377, 2019. doi: 10.1093/mnras/stz634.

[5] Ryuichi Takahashi, Masanori Sato, Takahiro Nishimichi, Atsushi Taruya, and Masamune Oguri. Revising the Halofit Model for the Nonlinear Matter Power Spectrum. *Astrophys. J.*, 761:152, 2012. doi: 10.1088/0004-637X/761/2/152.

[6] Alexander Mead, John Peacock, Catherine Heymans, Shahab Joudaki, and Alan Heavens. An accurate halo model for fitting non-linear cosmological power spectra and baryonic feedback models. *Mon. Not. Roy. Astron. Soc.*, 454(2):1958–1975, 2015. doi: 10.1093/mnras/stv2036.

[7] Robert E. Smith and Raul E. Angulo. Precision modelling of the matter power spectrum in a Planck-like Universe. 2018.

[8] Matteo Cataneo, Lucas Lombriser, Catherine Heymans, Alexander Mead, Alexandre Barreira, Sownak Bose, and Baojiu Li. On the road to percent accuracy: non-linear reaction of the matter power spectrum to dark energy and modified gravity. *Mon. Not. Roy. Astron. Soc.*, 488 (2):2121–2142, 2019. doi: 10.1093/mnras/stz1836.

[9] Katrin Heitmann, Earl Lawrence, Juliana Kwan, Salman Habib, and David Higdon. The Coyote Universe Extended: Precision Emulation of the Matter Power Spectrum. *Astrophys. J.*, 780:111, 2014. doi: 10.1088/0004-637X/780/1/111.

[10] Mischa Knabenhans et al. Euclid preparation: II. The EuclidEmulator – A tool to compute the cosmology dependence of the nonlinear matter power spectrum. *Mon. Not. Roy. Astron. Soc.*, 484:5509–5529, 2019. doi: 10.1093/mnras/stz197.

[11] Joseph DeRose, Risa H. Wechsler, Jeremy L. Tinker, Matthew R. Becker, Yao-Yuan Mao, Thomas McClintock, Sean McLaughlin, Eduardo Rozo, and Zhongxu Zhai. The Aemulus Project I: Numerical Simulations for Precision Cosmology. *Astrophys. J.*, 875(1):69, 2019. doi: 10.3847/1538-4357/ab1085.

[12] Siamak Ravanbakhsh, Junier Oliva, Sebastien Fromenteau, Layne C. Price, Shirley Ho, Jeff Schneider, and Barnabas Poczos. Estimating Cosmological Parameters from the Dark Matter Distribution. 2017.

[13] Janis Fluri, Tomasz Kacprzak, Alexandre Refregier, Adam Amara, Aurelien Lucchi, and Thomas Hofmann. Cosmological constraints from noisy convergence maps through deep learning. *Phys. Rev.*, D98(12):123518, 2018. doi: 10.1103/PhysRevD.98.123518.

[14] Justin Alsing, Tom Charnock, Stephen Feeney, and Benjamin Wandelt. Fast likelihood-free cosmology with neural density estimators and active learning. *Mon. Not. Roy. Astron. Soc.*, 488(3):4440–4458, 2019. doi: 10.1093/mnras/stz1960.

[15] Andrea Manrique-Yus and Elena Sellentin. Euclid-era cosmology for everyone: Neural net assisted MCMC sampling for the joint 3x2 likelihood. 2019.

[16] Marcel P. van Daalen, Joop Schaye, C. M. Booth, and Claudio Dalla Vecchia. The effects of galaxy formation on the matter power spectrum: A challenge for precision cosmology. *Mon. Not. Roy. Astron. Soc.*, 415:3649–3665, 2011. doi: 10.1111/j.1365-2966.2011.18981.x.

[17] Wojciech A. Hellwing, Matthieu Schaller, Carlos S. Frenk, Tom Theuns, Joop Schaye, Richard G. Bower, and Robert A. Crain. The effect of baryons on redshift space distortions

and cosmic density and velocity fields in the EAGLE simulation. *Mon. Not. Roy. Astron. Soc.*, 461(1):L11–L15, 2016. doi: 10.1093/mnrasl/slw081.

[18] Benjamin O. Mummery, Ian G. McCarthy, Simeon Bird, and Joop Schaye. The separate and combined effects of baryon physics and neutrino free-streaming on large-scale structure. *Mon. Not. Roy. Astron. Soc.*, 471(1):227–242, 2017. doi: 10.1093/mnras/stx1469.

[19] Volker Springel et al. First results from the IllustrisTNG simulations: matter and galaxy clustering. 2017.

[20] Nora Elisa Chisari, Mark L. A. Richardson, Julien Devriendt, Yohan Dubois, Aurel Schneider, M. C. Brun, Amandine Le, Ricarda S. Beckmann, Sebastien Peirani, Adrianne Slyz, and Christophe Pichon. The impact of baryons on the matter power spectrum from the Horizon-AGN cosmological hydrodynamical simulation. 2018.

[21] Marcel P. van Daalen, Ian G. McCarthy, and Joop Schaye. Exploring the effects of galaxy formation on matter clustering through a library of simulation power spectra. 2019.

[22] Simon Foreman, William Coulton, Francisco Villaescusa-Navarro, and Alexandre Barreira. Baryonic effects on the matter bispectrum. 2019.

[23] Alexandre Barreira, Dylan Nelson, Annalisa Pillepich, Volker Springel, Fabian Schmidt, Ruediger Pakmor, Lars Hernquist, and Mark Vogelsberger. Separate Universe Simulations with IllustrisTNG: baryonic effects on power spectrum responses and higher-order statistics. *Mon. Not. Roy. Astron. Soc.*, 488(2):2079–2092, 2019. doi: 10.1093/mnras/stz1807.

[24] E. Semboloni, H. Hoekstra, J. Schaye, M. P. van Daalen, and I. G. McCarthy. Quantifying the effect of baryon physics on weak lensing tomography. *Mon. Not. Roy. Astron. Soc.*, 417: 2020–2035, November 2011. doi: 10.1111/j.1365-2966.2011.19385.x.

[25] Irshad Mohammed, Davide Martizzi, Romain Teyssier, and Adam Amara. Baryonic effects on weak-lensing two-point statistics and its cosmological implications. 2014.

[26] C. Fedeli, E. Semboloni, M. Velliscig, M. Van Daalen, J. Schaye, and H. Hoekstra. The clustering of baryonic matter. II: halo model and hydrodynamic simulations. *JCAP*, 1408:028, 2014. doi: 10.1088/1475-7516/2014/08/028.

[27] Stijn N. B. Debackere, Joop Schaye, and Henk Hoekstra. The impact of the observed baryon distribution in haloes on the total matter power spectrum. 2019.

[28] Nora Elisa Chisari et al. Modelling baryonic feedback for survey cosmology. 2019. doi: 10.21105/astro.1905.06082.

[29] Aurel Schneider and Romain Teyssier. A new method to quantify the effects of baryons on the matter power spectrum. *JCAP*, 1512(12):049, 2015. doi: 10.1088/1475-7516/2015/12/049.

[30] Andreas J. Weiss, Aurel Schneider, Raphael Sgier, Tomasz Kacprzak, Adam Amara, and Alexandre Refregier. Effects of baryons on weak lensing peak statistics. 2019.

[31] Janis Fluri, Tomasz Kacprzak, Aurelien Lucchi, Alexandre Refregier, Adam Amara, Thomas Hofmann, and Aurel Schneider. Cosmological constraints with deep learning from KiDS-450 weak lensing maps. *Phys. Rev.*, D100(6):063514, 2019. doi: 10.1103/PhysRevD.100.063514.

[32] Aurel Schneider, Alexandre Refregier, Nicola Stoira, Mischa Knabenhans, Sebastian Grandis, Dominique Eckert, Joachim Stadel, and Romain Teyssier. Baryonic effects for weak lensing. Part II. Combination with X-ray data and extended cosmologies. 2019.

[33] Benjamin P. Moster, Thorsten Naab, and Simon D. M. White. Galactic star formation and accretion histories from matching galaxies to dark matter haloes. *Mon. Not. Roy. Astron. Soc.*, 428:3121, 2013. doi: 10.1093/mnras/sts261.

[34] Mario G. Abadi, Julio F. Navarro, Mark Fardal, Arif Babul, and Matthias Steinmetz.

Galaxy-Induced Transformation of Dark Matter Halos. *Mon. Not. Roy. Astron. Soc.*, 407: 435–446, 2010. doi: 10.1111/j.1365-2966.2010.16912.x.

[35] Shahab Joudaki et al. CFHTLenS revisited: assessing concordance with Planck including astrophysical systematics. *Mon. Not. Roy. Astron. Soc.*, 465(2):2033–2052, 2017. doi: 10.1093/mnras/stw2665.

[36] Shahab Joudaki et al. KiDS-450: Testing extensions to the standard cosmological model. *Mon. Not. Roy. Astron. Soc.*, 471(2):1259–1279, 2017. doi: 10.1093/mnras/stx998.

[37] H. Hildebrandt et al. KiDS-450: Cosmological parameter constraints from tomographic weak gravitational lensing. *Mon. Not. Roy. Astron. Soc.*, 465:1454, 2017. doi: 10.1093/mnras/stw2805.

[38] T. M. C. Abbott et al. Dark Energy Survey Year 1 Results: Cosmological Constraints from Galaxy Clustering and Weak Lensing. 2017.

[39] Chiaki Hikage et al. Cosmology from cosmic shear power spectra with Subaru Hyper Suprime-Cam first-year data. 2018.

[40] Ian G. Mccarthy, Simeon Bird, Joop Schaye, Joachim Harnois-Deraps, Andreea S. Font, and Ludovic Van Waerbeke. The BAHAMAS project: the CMB large-scale structure tension and the roles of massive neutrinos and galaxy formation. *Mon. Not. Roy. Astron. Soc.*, 476(3): 2999–3030, 2018. doi: 10.1093/mnras/sty377.

[41] G. Hinshaw et al. Nine-Year Wilkinson Microwave Anisotropy Probe (WMAP) Observations: Cosmological Parameter Results. *Astrophys. J. Suppl.*, 208:19, 2013. doi: 10.1088/0067-0049/208/2/19.

[42] P. A. R. Ade et al. Planck 2013 results. XVI. Cosmological parameters. *Astron. Astrophys.*, 571:A16, 2014. doi: 10.1051/0004-6361/201321591.

[43] D. N. Spergel et al. Wilkinson Microwave Anisotropy Probe (WMAP) three year results: implications for cosmology. *Astrophys. J. Suppl.*, 170:377, 2007. doi: 10.1086/513700.

[44] E. Komatsu et al. Seven-Year Wilkinson Microwave Anisotropy Probe (WMAP) Observations: Cosmological Interpretation. *Astrophys. J. Suppl.*, 192:18, 2011. doi: 10.1088/0067-0049/192/2/18.

[45] J. G. Stadel. *Cosmological N-body simulations and their analysis*. PhD thesis, UNIVERSITY OF WASHINGTON, 2001.

[46] Douglas Potter, Joachim Stadel, and Romain Teyssier. PKDGRAV3: Beyond Trillion Particle Cosmological Simulations for the Next Era of Galaxy Surveys. 2016.

[47] S. R. Knollmann and A. Knebe. AHF: Amiga's Halo Finder. *Astrophys. J. Supp.*, 182:608–624, June 2009. doi: 10.1088/0067-0049/182/2/608.

[48] Stefano Marelli and Bruno Sudret. *UQLab: A Framework for Uncertainty Quantification in Matlab*, pages 2554–2563. doi: 10.1061/9780784413609.257. URL https://ascelibrary.org/doi/abs/10.1061/9780784413609.257.

[49] D. N. Limber. The Analysis of Counts of the Extragalactic Nebulae in Terms of a Fluctuating Density Field. *Astrophys. J.*, 117:134, January 1953. doi: 10.1086/145672.

[50] Christopher M. Hirata and Uroš Seljak. Intrinsic alignment-lensing interference as a contaminant of cosmic shear. *Phys. Rev. D*, 70(6):063526, Sep 2004. doi: 10.1103/PhysRevD.70.063526.

[51] Sarah Bridle and Lindsay King. Dark energy constraints from cosmic shear power spectra: impact of intrinsic alignments on photometric redshift requirements. *New J. Phys.*, 9:444, 2007. doi: 10.1088/1367-2630/9/12/444.

[52] T. Kacprzak et al. Monte Carlo Control Loops for cosmic shear cosmology with DES Year 1. 2019.

[53] Daniel J. Eisenstein and Wayne Hu. Baryonic Features in the Matter Transfer Function. *Astrophysical Journal*, 496:605–614, March 1998. doi: 10.1086/305424.

[54] Alexandre Refregier, Lukas Gamper, Adam Amara, and Lavinia Heisenberg. PyCosmo: An Integrated Cosmological Boltzmann Solver. *Astron. Comput.*, 25:38–43, 2018. doi: 10.1016/j.ascom.2018.08.001.

[55] Oliver Hahn and Tom Abel. Multi-scale initial conditions for cosmological simulations. *Monthly Notices of the RAS*, 415:2101–2121, August 2011. doi: 10.1111/j.1365-2966.2011.18820.x.

[56] P. A. R. Ade et al. Planck 2015 results. XXIV. Cosmology from Sunyaev-Zeldovich cluster counts. *Astron. Astrophys.*, 594:A24, 2016. doi: 10.1051/0004-6361/201525833.

[57] N. Aghanim et al. Planck 2018 results. VI. Cosmological parameters. 2018.

[58] Gary Steigman. Primordial Nucleosynthesis in the Precision Cosmology Era. *Ann. Rev. Nucl. Part. Sci.*, 57:463–491, 2007. doi: 10.1146/annurev.nucl.56.080805.140437.

[59] Joël Akeret, Sebastian Seehars, Adam Amara, Alexandre Refregier, and André Csillaghy. CosmoHammer: Cosmological parameter estimation with the MCMC Hammer. *arXiv e-prints*, art. arXiv:1212.1721, Dec 2012.

[60] Daniel Foreman-Mackey, David W. Hogg, Dustin Lang, and Jonathan Goodman. emcee: The MCMC Hammer. *PASP*, 125(925):306, Mar 2013. doi: 10.1086/670067.

[61] Y. P. Jing, Pengjie Zhang, W. P. Lin, L. Gao, and V. Springel. The influence of baryons on the clustering of matter and weak lensing surveys. *Astrophys. J.*, 640:L119–L122, 2006. doi: 10.1086/503547.

[62] Douglas H. Rudd, Andrew R. Zentner, and Andrey V. Kravtsov. Effects of Baryons and Dissipation on the Matter Power Spectrum. *Astrophys. J.*, 672:19–32, 2008. doi: 10.1086/523836.

[63] Hung-Jin Huang, Tim Eifler, Rachel Mandelbaum, and Scott Dodelson. Modeling baryonic physics in future weak lensing surveys. 2018.

[64] J. Hartlap, Patrick Simon, and P. Schneider. Why your model parameter confidences might be too optimistic: Unbiased estimation of the inverse covariance matrix. *Astron. Astrophys.*, 2006. doi: 10.1051/0004-6361:20066170. [Astron. Astrophys.464,399(2007)].

[65] Elena Sellentin and Alan F. Heavens. Parameter inference with estimated covariance matrices. *Mon. Not. Roy. Astron. Soc.*, 456(1):L132–L136, 2016. doi: 10.1093/mnrasl/slv190.

[66] Andrea Zonca, Leo Singer, Daniel Lenz, Martin Reinecke, Cyrille Rosset, Eric Hivon, and Krzysztof Gorski. healpy: equal area pixelization and spherical harmonics transforms for data on the sphere in python. *Journal of Open Source Software*, 4(35):1298, March 2019. doi: 10.21105/joss.01298. URL https://doi.org/10.21105/joss.01298.

[67] Dan Foreman-Mackey, Will Vousden, Adrian Price-Whelan, Matt Pitkin, Victor Zabalza, Geoffrey Ryan, Emily, Michael Smith, Gregory Ashton, Kelle Cruz, Wolfgang Kerzendorf, Thomas A Caswell, Stephan Hoyer, Kyle Barbary, Ian Czekala, Hanno Rein, Eric Gentry, Brendon J Brewer, and David W Hogg. Corner.Py: Corner.Py V2.0.0. art. 10.5281/zenodo.53155, May 2016. doi: 10.5281/zenodo.53155.

[68] Peter S. Behroozi, Risa H. Wechsler, and Charlie Conroy. The Average Star Formation Histories of Galaxies in Dark Matter Halos from z =0-8. *Astrophys. J.*, 770:57, 2013. doi: 10.1088/0004-637X/770/1/57.

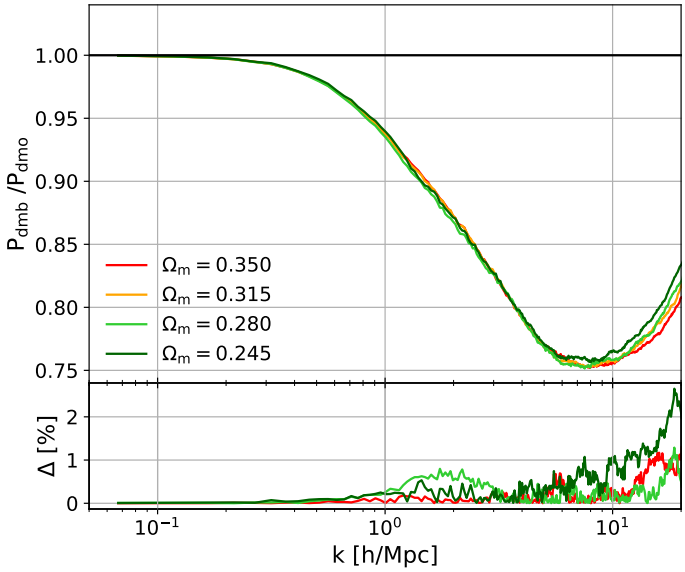

Figure 12. Changes in the baryonic power suppression if we use N-body simulations with varying Ω_m while keeping Ω_m constant in the formalism of the baryonic correction model (i.e. Eq. 2.7). All changes stay below one percent for $k < 10$ h/Mpc (see lower panel).

A More about the baryonic emulator

In this appendix we give some more details about the construction and the testing of the *baryonic emulator* presented in Sec. 2.

A.1 Reference N-body simulation for the emulator

In Section 2.2 of the main text we have argued that, for building the baryonic emulator, it is sufficient to only vary the parameters of the baryonic correction model while keeping a fixed background N-body simulation. This assumption allowed us to increase the experimental design to $N_{\rm ED} = 1000$, thereby improving the accuracy of the emulator to a higher level. In this Appendix, we provide further evidence as to why this assumption is valid.

Fig. 2 of the main text shows that the baryonic suppression signal does not depend on the cosmological parameter h_0, σ_8, and n_s while it is affected by the variation of the cosmic baryon fraction $f_b = \Omega_b/\Omega_m$. This is not surprising, since the baryonic correction model directly depends on f_b, whereas all other cosmological parameter only come in through changes of the underlying N-body simulation. However, since we are only emulating the ratio of two power spectra (with the same underlying cosmology), these effects cancel out.

In Fig. 12 we show that if Ω_m (and therefore f_b) is varied in the underlying N-body simulation without changing f_b in the formalism of the baryonic correction model, then the baryonic suppression signal is only affected at the sub-percent level below $k \sim 10$ h/Mpc. Conversely, this means that any cosmology dependence of the baryonic suppression effect comes from Eq. (2.7) (that explicitly depends on f_b) and not from the underlying N-body simulation. As a consequence, we can use the same simulation to construct our emulator without compromising its accuracy at a significant level.

Sample	f_b	$\log M_c$	μ	$\theta_{\rm ej}$	$\eta_{\rm star}$	$\eta_{\rm cga}$
0	0.207	16.601	0.173	3.308	0.314	0.569
1	0.172	15.197	0.939	5.102	0.370	0.556
2	0.132	13.529	0.339	6.605	0.360	0.625
3	0.185	14.419	0.498	2.007	0.267	0.680
4	0.150	15.985	0.797	7.354	0.209	0.638
5	0.162	12.801	0.583	4.136	0.236	0.532

Table 3. Parameter values of the sample on which the *baryonic emulator* is tested. The test sample is randomly selected based on the LHC sampling method and does not coincide with the sample points from the experimental design (which is used to construct the emulator).

A.2 Emulator performance

In Sec. 2.3 of the main text, we have presented the *baryonic emulator*, quantified its overall precision (see Fig. 4), and we have shown a comparison between emulator and baryonic correction model for two selected sample points in the parameter space (Fig. 3). In the present Appendix, we give more details about the performance of the emulator, also showing the results from the remaining four sample points that make up the test sample of our emulator.

The test sample has been randomly selected using the optimised latin hypercube sampling (LHS) method. Note that the test sample does not coincide with the experimental design (ED) on which the emulator has been constructed. The parameter values of the six sample points are given in Table 3.

In Fig. 13 we show a comparison of the relative power spectra obtained from the baryonic emulator (dashed) and directly from the baryonic correction model (solid) for each of the six test-sample points. In order to provide a good overview, we again include the power spectra illustrated in Fig. 3 of the main text. However, this time we not only show the redshifts ($z_{\rm emu}$) on which the emulator has been constructed ($z_{\rm emu} = 0, 0.5, 1.0, 1.5, 2.0$), but also intermediate redshifts ($z_{\rm interp} = 0.234, 0.767, 1{,}281, 1.798$), where the emulation code interpolates between the emulated values. The results from the sample points 0-5 are arranged from top-left to bottom-right (aways one panel showing the power spectra at $z_{\rm emu}$ and one at $z_{\rm interp}$). The first and the third panel of the top row are identical to Fig. 3.

From Fig. 13 we conclude that the emulation is well performed within a $1-2$ percent error margin in most of the considered cases. However, there are some outliers at some specific redshifts and k-modes, where the errors of the emulator increases to the $2-3$ percent level. This qualitative conclusion is in agreement with the more quantitative error analysis of Sec. 2.3.

Yet another way to illustrate the performance of the *baryonic emulator* is to visualise the errors per redshift z and not per sample point. The results are presented in Fig. 14. In terms of maximum absolute error, the emulation performance is worst at redshift 0 (with $\max(\mathrm{P_{emu}/P_{true}} - 1) = 3.296$) and best at redshift 2 (with $\max(\mathrm{P_{emu}/P_{true}} - 1) = 1.512$).

B Cosmological inference: why 3 (and not 5) baryonic parameters?

Both the *baryonic emulator* and the underlying *baryonic correction model* are based on 5 baryonic parameters (M_c, μ, $\theta_{\rm ej}$, $\eta_{\rm star}$, $\eta_{\rm cga}$). However, the forecast analysis presented in Sec. 4 is limited to the variation of the gas parameters (M_c, μ, $\theta_{\rm ej}$), whereas the stellar parameters ($\eta_{\rm star}$, $\eta_{\rm cga}$) are fixed to their benchmark values.

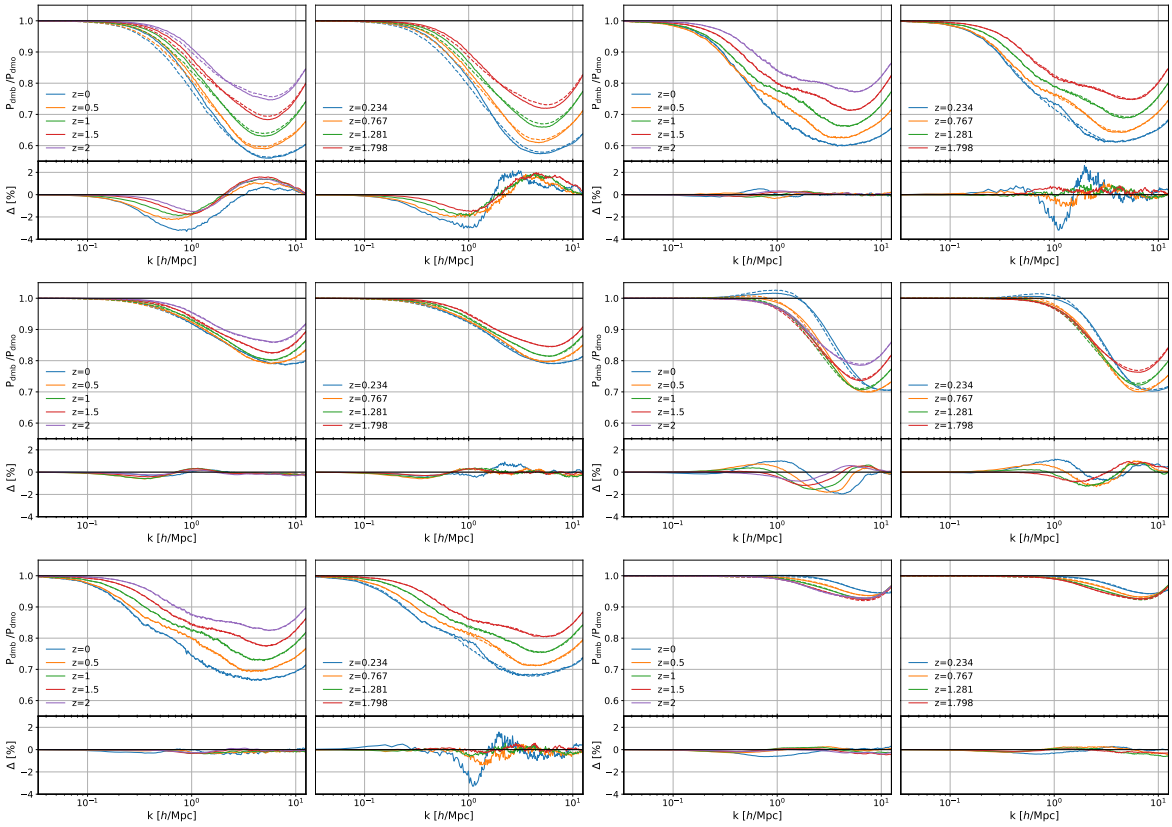

Figure 13. Comparison between the *baryonic correction model* and the *baryonic emulator* for the six sample points from the emulator test-set. Sample one two six are plotted from top left to bottom right (always two panels per sample showing different redshifts). The first and the third pair of panels referring to sample 1 and 3 have been shown in the main text but are plotted again to allow for a better comparison. The solid lines show the baryonic power suppression from the BC model, the dashed lines are the results from the emulator. All parameter values for each sample are summarised in Table 3.

In the main text, we have justified the restriction to 3 baryonic parameters with the fact that the stellar parameters ($\eta_{\rm star}$, $\eta_{\rm cga}$) have a comparably small effect on the matter power spectrum that only becomes apparent at relatively small scales (see for example Fig. 2 of S19). Furthermore, the parameters are already well constrained with the observed luminosity function coupled to dark matter theory via the abundance matching techniques [e.g. Refs 33, 68]. Note that abundance matching galaxies to haloes is not independent of cosmology. However, we do not expect substantial changes of $\eta_{\rm star}$, $\eta_{\rm cga}$ for reasonable modifications of cosmological parameter values (for example within the prior range of our analysis).

In this Appendix, we test the effects of varying $\eta_{\rm star}$ and $\eta_{\rm cga}$ (together with the other baryonic cosmological and intrinsic-alignment parameters) on the posterior contours of our forecast analysis. We thereby assume the flat priors $\eta_{\rm star} \in [0.2, 0.4]$ and $\eta_{\rm cga} \in [0.5, 0.7]$. All other priors are given in Table 2 of the main text.

Fig. 15 shows the resulting posterior contours for the five cosmological parameters (Ω_m, Ω_b, σ_8, h_0, n_s). The black lines indicate the true cosmology assumed when for the construction of the mock observations. The red contours illustrate the result from the original forecast analysis with 3 baryonic parameters (M_c, μ, $\theta_{\rm ej}$), already shown in Fig. 7 and 11 from the

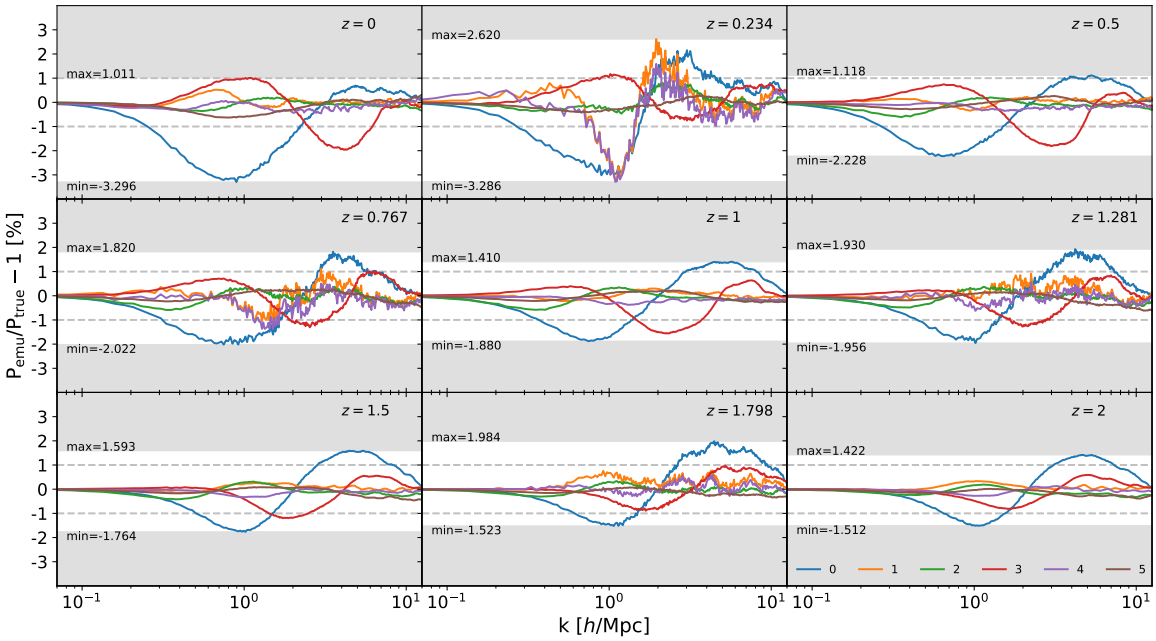

Figure 14. Relative emulation error ($P_{emu}/P_{true} - 1$) at different redshifts (from top-left to bottom-right) for the 6 points of the test sample (different colours). The dashed lines in each plot represent the $\pm 1\%$ error range. The shaded region highlight the maximum and the minimum relative error at each k-mode and for each redshift.

main text. The black contours, on the other hand, correspond to the extended cosmological inference analysis including all 5 baryonic parameters (M_c, μ, θ_{ej}, η_{star}, η_{cga}). The red and black contour areas are very similar. Although we added two new parameters, the black contours have not become larger than the red ones. This means that varying stellar parameters (η_{star}, η_{cga}) has no noticeable effect on the cosmological parameter estimates. We therefore conclude that fixing the stellar parameters to their default values is a valid approximation for future stage-IV weak-lensing surveys.

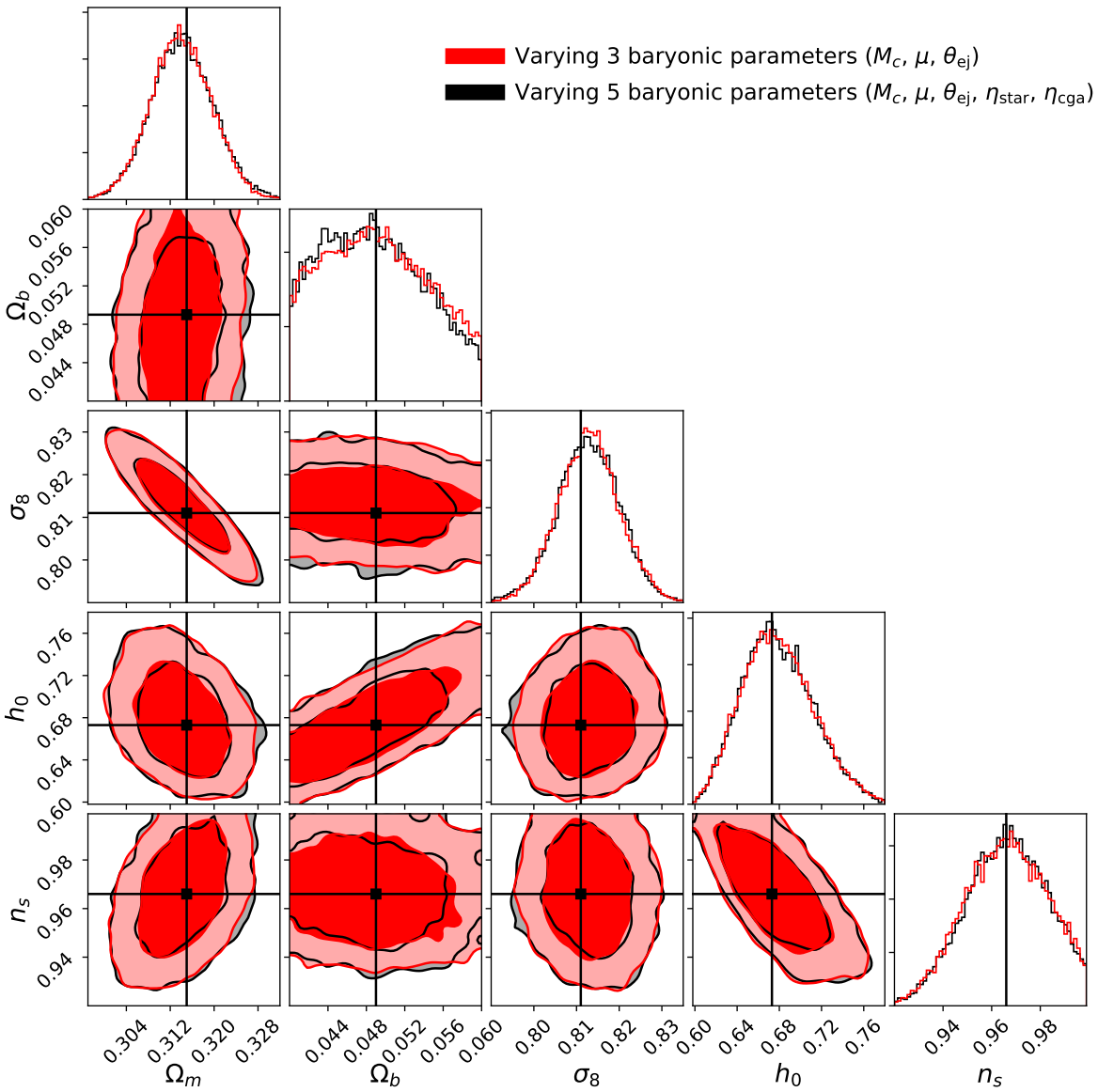

Figure 15. Comparison of the posterior contours when we extend the number of free baryonic parameters from 3 (red) to 5 (black). The former corresponds to the default setup applied in our forecast analysis of Paper I and II. The latter includes all free parameters originally proposed in the S19. The black lines indicate the true cosmology of the mock sample.